THE ASTROPHYSICAL JOURNAL, 384:423–432, 1992 January 10

ELLIPTICAL GALAXIES WITH DARK MATTER. I. SELF-CONSISTENT MODELS

G. BERTIN AND R. P. SAGLIA[1]
Scuola Normale Superiore, Piazza dei Cavalieri 7, 56126 Pisa, Italy
AND
M. STIAVELLI
European Southern Observatory, Karl-Schwarzschild-Strasse 2, D-8046 Garching bei München, Germany
Received 1991 January 29; accepted 1991 July 22

ABSTRACT

A large survey of two-component, spherically symmetric, collisionless, self-consistent models is carried out with the aim of studying elliptical galaxies embedded in massive dark halos. Although many factors and options are explored in quantitative detail, the main focus is on a family of models where the luminous component is mostly isotropic inside the half-light radius and the dark component is slightly warmer (and normally more diffuse) than the luminous component, consistent with the picture that ellipticals were generically formed as a result of collisionless collapse (or merging) in the presence of cold/warm dark matter. The constraints imposed by self-consistency are found to be quite complex, but a few important features (such as limits on the amount of dark matter inside the half-light radius in terms of observed quantities and a characterization of the physical parameter space) are clarified by a proper use of the Jeans equations and of the virial theorem. In spite of the variety of kinematical profiles realized in our self-consistent models, we note a natural "conspiracy" to support realistic photometries, that is, luminosity profiles consistent with the $R^{1/4}$ law. Within our main family of models, we develop the concept of "minimum-halo models" as a way to fit a given set of data by minimizing the request of dark matter. This paper, where many of the results are illustrated in terms of projected quantities for a direct application to observed objects, forms the theoretical basis for a systematic study of photometric and kinematical properties of elliptical galaxies that may give quantitative estimates on the amount of dark matter present in these systems.

Subject headings: dark matter — galaxies: elliptical and lenticular, cD — galaxies: fundamental parameters — galaxies: kinematics and dynamics

1. INTRODUCTION

Dynamical evidence for the presence of dark matter in galaxies is usually claimed when models with stellar components characterized by constant mass-to-light ratios prove inadequate when confronted with observations. The possibility of radial gradients in the M/L ratios for the stellar components is generally discarded especially because large color gradients are not observed (Peletier et al. 1990; Franx & Illingworth 1990). For spiral galaxies this point of view leads to the construction of "maximum-disk models" (see van Albada & Sancisi 1986); in general, significant amounts of dark matter are required only when the models are confronted with H I data well beyond the optical disk, as in the clear case of NGC 3198 (van Albada et al. 1985).

For elliptical galaxies the situation is less clear (see Sarazin 1987; Sancisi & van Albada 1987). Although one-component stellar dynamical models so far appear to provide a good zeroth-order description of current data (see, e.g., Bertin, Saglia, & Stiavelli 1988; van der Marel, Binney, & Davies 1990; Binney, Davies, & Illingworth 1990; Efstathiou, Ellis, & Carter 1982), the kinematical data considered for these galaxies are mostly restricted to the region inside the half-light radius. Indeed, nonstellar kinematic indicators that are sometimes available on a larger scale (such as X-rays or H I; see Forman et al. 1979; Fabricant, Lecar, & Gorenstein 1980; Canizares, Fabbiano, & Trinchieri 1987; Raimond et al. 1981; van Gorkom et al. 1986; Schweizer, van Gorkom, & Seitzer 1989; Lees, van Gorkom, & Knapp 1990) tend to favor the view that dark matter is present also in ellipticals. In particular, some cases of flat H I rotation curves have been found, raising the interesting possibility of a "kinematic conspiracy" similar to that found in spiral galaxies.

This brief discussion gives the primary motivation for this paper, that is, the construction of self-consistent two-component models of elliptical galaxies where one component is supposed to represent the stars and the other the dark matter. The theoretical issue addressed here in great detail is the role of self-consistency in constraining the properties of the models. Note that because of the Gauss theorem, we expect the distribution of dark matter, if diffuse, to suffer more from the influence of luminous matter than vice versa. On the other hand, if we are going to invoke the presence of dark matter based on some kinematical signatures on the stellar component, such as a relatively flat velocity dispersion profile (see Saglia, Bertin, & Stiavelli 1992, hereafter Paper II), we should consider the possibility that dark matter may be present in significant amounts inside the half-light radius and thus affect the distribution of the stellar component. Therefore, it is not clear *why* the luminosity profile should always conform to the universal $R^{1/4}$ law (de Vaucouleurs 1948, 1953) rather than being distorted depending on the amount of dark matter present; this seems to be a kind of "photometric conspiracy" operating if elliptical galaxies do indeed contain dark matter (Bertin, Saglia, & Stiavelli 1989). In fact, it is somewhat of a miracle that the realization and survival of the $R^{1/4}$ profile happen to occur for a large subset of the parameter space

[1] Postal address: Landessternwarte, D-6900 Heidelberg-Koenigstuhl, Germany.

defining our simple but fully self-consistent models (see especially following § 5).

There are two possibilities for distributing dark matter differently from the luminous component. One way is to consider dark halos with a *different shape* (see the extreme case of spiral galaxies where dark matter is thought to have a spheroidal distribution in contrast with the stellar disk); the other is to have a distribution with a *different radial scale length* (in particular a larger scale length). Although the first possibility raises many interesting questions, in this paper we shall address only the second aspect which can be tackled adequately already in the simplified context of spherical models.

The paper is organized in the following way. First we choose a form for the distribution function describing both components and justify the merits and limitations of our choice (§ 2). Then we discuss the properties of the large parameter space that characterizes the family of models of main interest (§ 3) and present our survey of models which leads to the construction of a "data base" of 2939 fully self-consistent models within the main family (§ 4); we illustrate the intrinsic and observable properties of the models found. In § 5, we develop the concept of *minimum-halo models*, derive a few simple expressions that relate the amount of dark matter inside the half-light radius to the observed stellar velocity dispersion profile, and discuss the properties of models with good luminosity profiles ("photometric conspiracy") in the physical parameter space. In Appendix A some of the adopted numerical techniques are briefly outlined with reference to the numerical accuracy that has been obtained, and to the completeness of the survey. Appendix B is devoted to an exploration of some issues that are beyond the main goal of this article, that is, rotation and properties of some models that are outside the main survey.

2. CHOICE OF THE DISTRIBUTION FUNCTION FOR THE TWO COMPONENTS

With the aim of studying the effects on the observable quantities of the introduction of a dark component in an equilibrium model of elliptical galaxy, we have constructed a family of fully self-consistent two-component models. In the physical picture where the two components are both collisionless and have undergone similar dynamical processes during galaxy formation starting from different initial conditions, we should consider two distribution functions (that may be taken to be of the same form, but to imply different scale lengths and masses for the dark and the luminous component), keeping in mind the empirical constraint that the luminous component should follow the $R^{1/4}$ law. In addition, given the little evidence available so far for the presence of dark matter inside elliptical galaxies, we would like to explore a range of models where the dark component is progressively "turned on" over a well-justified reference model with no dark matter. One such reference case is that of the f_∞-models (Bertin & Stiavelli 1984), which we have found to possess interesting properties in relation to the statistical mechanics of galaxy formation (Stiavelli & Bertin 1987) and to the detailed fit of observed galaxies (see Bertin et al. 1988). It should be noted that this approach is preferred over the simpler scheme of embedding a specified model for the luminous component in a "frozen" spherical halo since it enables one to investigate the problem of "photometric conspiracy" and to consider models where the two components have comparable masses (within the region where stellar kinematics indicators can be measured) and are thus expected to heavily influence each other.

Therefore, we start out with a family of two-component spherical models where each component is described by a distribution function of the f_∞-form:

$$f_L = A_L(-E)^{3/2} \exp\left[-a_L E - c_L J^2/2\right], \quad (1)$$

$$f_D = A_D(-E)^{3/2} \exp\left[-a_D E - c_D J^2/2\right], \quad (2)$$

where $E = v^2/2 + \Phi$ is the specific energy and $J^2 = r^2 v_T^2$ is the specific angular momentum. The distribution functions f_L and f_D are taken to vanish for $E \geq 0$. With this choice, we can imagine varying the "temperature," the amount, and the radial scale of the dark matter by changing the ratios a_D/a_L, A_D/A_L, and c_D/c_L.

An extensive survey is required to study how the physical properties of the models are constrained by self-consistency, which is imposed by the Poisson equation for the gravitational potential Φ shared by the two components.

This is a survey of models with four free parameters. We start with seven dimensional parameters a_L, a_D, c_L, c_D, A_L, A_D, and the value of the central gravitational potential $\Phi(0)$. Two of these can be fixed by choosing the scale length and the total mass of the model. A third parameter can be eliminated by solving the Poisson equation under the appropriate boundary conditions. A convenient choice of dimensionless parameters is a_D/a_L, c_D/c_L, A_D/A_L, $\Psi = -a_L\Phi(0)$, which are taken to be positive. We discuss their physical meaning in the next section.

Taking into account the existence of "conjugate" models, that is, those that are obtained by exchanging the luminous with the dark component, for a complete survey of solutions it is sufficient to take $a_D/a_L < 1$. Models with $a_D/a_L = 1$ and $c_D/c_L = 1$, or models with either A_L or A_D equal to zero are all equivalent to the reference one-component f_∞-models. Here we do not survey models with $\Psi < 0$ or $a_D < 0$ because they are expected to be dynamically unstable. (In fact, models with "negative temperature" [Merritt, Tremaine, & Johnstone 1989] are characterized by a very high degree of radial anisotropy which makes them violently unstable even in the presence of a halo [Stiavelli & Sparke 1991].)

We should stress that the models considered in this paper while allowing for some variations in the distribution of stellar orbits, do *not* have *arbitrary* "pressure" profiles for the two components; in particular, they are all isotropic in the central parts and dominated by radial orbits in the outer regions. This choice of focus, which excludes many other options, such as models dominated by circular orbits, is made on purpose because we would like to study models consistent with the most widely accepted ideas on galaxy formation, that is, dissipationless collapse (van Albada 1982) and merging (see, e.g., Barnes 1989). On the other hand, the detailed *analytical form* of distribution function for the models selected by the physical picture that we adopt is by no means unique (Bertin & Stiavelli 1989). Thus, in order to test the generality of our approach we have also considered in some detail models described by other distribution functions that also incorporate the essential features of collisionless collapse (Stiavelli & Bertin 1987, equation 9). Some of these models will be used in Paper II to test our luminous-dark decomposition on "simulated observations."

In conclusion, we do not claim full completeness of analysis in our investigation of two-component models, but only physical plausibility and sufficient generality of the models that we focus on. This paper will then provide the theoretical basis for

one way of modeling elliptical galaxies and measuring M/L ratios as illustrated in the following Paper II.

3. THE PARAMETER SPACE FOR THE $(f_\infty + f_\infty)$ MODELS AND ITS PHYSICAL MEANING

The dimensionless parameters a_D/a_L, c_D/c_L, A_D/A_L, and Ψ are directly related to the physical properties of the model. We define $\bar{\sigma}_r(r)$, $\bar{\sigma}_T(r)$, and $\bar{\sigma}(r) = \sqrt{(\bar{\sigma}_r^2 + \bar{\sigma}_T^2)/3}$ as the radial, tangential, and unprojected (average over the spatial directions) velocity dispersion, respectively, and $\sigma(R)$ as the velocity dispersion of a given component projected along the line of sight at projected distance R from the center.

For high values of Ψ ($\Psi \gg 1$, $\Psi \gg a_L/a_D$) we obtain the following relations for the central velocity dispersion and density ratios:

$$\frac{\bar{\sigma}_L(0)}{\bar{\sigma}_D(0)} \sim \left(\frac{a_D}{a_L}\right)^{1/2}, \tag{3}$$

$$\frac{\rho_L(0)}{\rho_D(0)} \sim \frac{A_L}{A_D}\left(\frac{a_D}{a_L}\right)^{3/2} \exp\left[\Psi\left(1 - \frac{a_D}{a_L}\right)\right]. \tag{4}$$

Note that for $0.25 \leq a_D/a_L \leq 1$, which is the range considered in the survey of models described in the next section, we have $\bar{\sigma}_D(0) \leq 1.75\bar{\sigma}_L(0)$. In a *hot* dark matter scenario, the dark component should have a velocity dispersion much higher than that of the luminous component. Thus, a very low value of a_D/a_L is needed to produce an $(f_\infty + f_\infty)$-model with this property. In contrast, models with $a_D/a_L \lesssim 1$ have a $\bar{\sigma}_L(0)/\bar{\sigma}_D(0)$ ratio similar to what we can expect in a *cold* or *warm* dark matter scenario.

The value of c_D/c_L fixes the ratio r_{aL}/r_{aD} of the anisotropy radii of the luminous and of the dark components. The anisotropy radius r_a is defined as the location where the anisotropy parameter $\alpha(r) = 2 - \bar{\sigma}_T^2(r)/\bar{\sigma}_r^2(r)$ equals unity (cf. van Albada 1982). In contrast with the estimates given by equations (3)–(4), the relation between c_D/c_L and the ratio r_{aL}/r_{aD} depends on the global properties of the self-consistent solutions. On the basis of the survey of the $(f_\infty + f_\infty)$ models to be described in the next section, we find that a very good power-law fit for the anisotropy ratio r_{aL}/r_{aD} is given by the relation:

$$\frac{r_{aL}}{r_{aD}} \approx 1.1\left(\frac{c_D}{c_L}\right)^{0.8}. \tag{5}$$

Once the Poisson equation has been solved, all the physical properties of the models can be derived; a synthetic description of the global features of these models can be given in terms of a few physical parameters in addition to r_{aL}/r_{aD}, such as:

1. The ratio r_L/r_D of the half-mass radii of the two components.
2. The ratio M_L/M_D of the total masses of the two components.
3. The flatness parameter of the (unprojected) velocity dispersion profile of the luminous component $\bar{\sigma}_L(3r_L)/\bar{\sigma}_L(0)$.
4. The flatness parameters of the circular velocity profile $V(3r_L)/V_{\max}$, where $V(r) = \sqrt{r(d\Phi/dr)}$ measures the gravitational force field of the model with maximum value $V_{\max}$.
5. The "luminosity" parameter:

$$\chi_{10}^2 = \sum_{r=r_L/10}^{10r_L} \left[\frac{\rho_L(r) - \rho_J(r)}{\rho_L(r)}\right]^2 \Big/ N, \tag{6}$$

which we introduce in order to measure the departures from the $R^{1/4}$ law of the density of the luminous component. In equation (6) N is the number of points considered, and for simplicity the density consistent with the $R^{1/4}$ profile is approximated by means of the function ρ_J (Jaffe 1983), scaled to have the same half-mass radius and the same density at such radius.

4. A SURVEY OF $(f_\infty + f_\infty)$ MODELS

We have solved the Poisson equation numerically under the natural boundary conditions (see Saglia 1990), using the algorithms described in Appendix A, for 10,000 values of the parameters a_D/a_L, c_D/c_L, A_D/A_L, Ψ. For a given set of dimensional parameters a_D, a_L, A_D, A_L, Ψ/a_L, and c_D, our code computes a value of c_L (if it exists) which produces an equilibrium model satisfying the virial theorem with a given accuracy ($|1 - 2K/|W|| < 10^{-4}$).

The explored region of the parameter space is defined as follows. Twenty different values of c_D and A_D ($30 \leq c_D \leq 600$, $1 \leq A_D \leq 39$) and five different values of a_D and Ψ ($0.5 \leq a_D \leq 1.5$, $8 \leq \Psi \leq 24$), all uniformly spaced, have been considered, setting our units so that $A_L = 1$, $a_L = 2$ and the gravitational constant $G = 1/4\pi$. The adopted grid covers a wide region of the allowed parameter space, with central density ratio $\rho_L(0)/\rho_D(0)$ ranging from 10^{-1} to 10^7. In particular, high values of Ψ have been focused on, since the luminous component of the $(f_\infty + f_\infty)$ models follows the $R^{1/4}$ law only if it is sufficiently centrally concentrated.

4.1. *The Set of Accepted Solutions: "Normal" and "Reverse" Models*

Out of the 10,000 models calculated, only 2939 solutions were accepted. In the remaining cases, the numerical routines either did not converge or led to solutions that were judged to be inaccurate.

We define as *normal*, models with $r_L/r_D < 1$, and as *reverse*, models with $r_L/r_D > 1$. A *normal* model with parameters a_D/a_L, c_D/c_L, A_D/A_L, and Ψ is "conjugate" to the *reverse* model with parameters a_L/a_D, c_L/c_D, A_L/A_D, and $\Psi a_D/a_L$. We found 852 *normal* models and 2087 *reverse* models. *Normal* models are interesting for the description of elliptical galaxies with dark matter, since they possess a highly concentrated luminous component and a more diffuse dark halo. *Reverse* models have in general a dark component with small or insignificant mass. Thus, in their observable properties they are very similar to the one-component f_∞-models with the same value of Ψ.

Some properties of the equilibrium models can be described by the following interpolation formulae:

$$\frac{r_L}{r_D} \approx 1.6\left(\frac{c_D}{c_L}\right)^{0.45}\left(\frac{a_D}{a_L}\right)^{0.8}\left(\frac{A_D}{A_L}\right)^{-0.3}, \tag{7}$$

$$\frac{M_L}{M_D} \approx 1.8\left(\frac{c_D}{c_L}\right)^{0.3}\left(\frac{a_D}{a_L}\right)^{-0.2}\left(\frac{A_D}{A_L}\right)^{-0.8}. \tag{8}$$

These formulae hold essentially for all values of Ψ for the normal models of our survey, although with a larger scatter with respect to relation (5).

The 2939 accepted models described above cover a wide region of the physical parameter space. The $r_L/r_D - M_L/M_D$ plane is covered almost uniformly, except that models with low r_L/r_D ratios have only low M_L/M_D values. It is possible to construct models with a less massive and more diffuse dark component by choosing lower values of the parameter a_D/a_L ($a_D/a_L < 0.25$). In Figure 1 we illustrate the range of properties

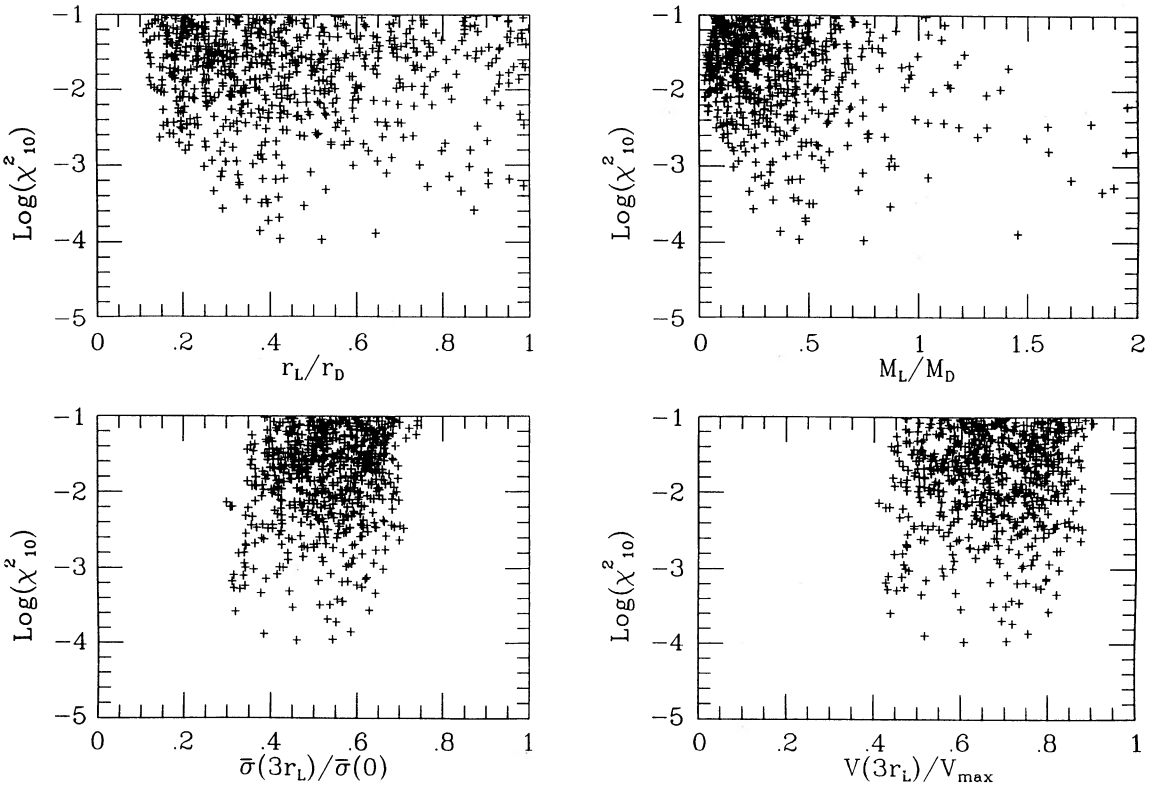

FIG. 1.—"Luminosity parameter" is plotted vs. some key mass and kinematical quantities for the two-component *normal* models

probed by our family of models for other physical parameters as a function of the value of the χ^2_{10} parameter. From these plots it follows that we have constructed a set of models with a luminous component following the $R^{1/4}$ law ($\log \chi^2_{10} < -1$) and with a large spread in the dark mass content and in the mass distribution. From the same plots it follows that a wide class of velocity dispersion profiles has been obtained, from the steeply declining case [$\bar{\sigma}_L(3r_L)/\bar{\sigma}_L(0) = 0.3$], to the nearly flat behavior [$\bar{\sigma}_L(3r_L)/\bar{\sigma}_L(0) = 0.7$]. Finally, these models show quite a variety of circular velocity profiles. In conclusion, our set of two-component models can describe elliptical galaxies with a moderately massive and diffuse dark halo with slowly declining velocity dispersion profiles and nearly flat circular velocity profiles.

4.2. *Three Representative Classes of Two-Component Models*

The models that we have constructed can be roughly grouped in three classes on the basis of the relative importance and distribution of their luminous and dark components. These classes are well illustrated by three representative models ($N = 402$, 1857, and 9382; see Fig. 2).

The *reverse* model $N = 402$ ($\Psi = 12$, $a_D = 0.5$, $A_D = 1$, $c_D = 150$, $c_L = 10$) has a small amount of dark matter ($M_L/M_D = 8.5$) and thus is very similar to the one-component $\Psi = 12$ model. The densities of the luminous and dark components decrease as r^{-4} in the outer regions ($r > r_L$, $r_L = 0.41$, $r_L/r_D = 1.4$), while for $10^{-3} r_L < r < r_L$ we have $\rho_L \sim r^{-2}$, $\rho_D \sim r^{-1.1}$. In the very central regions ($r < 10^{-3} r_L$) there is a flat core. The model has a Keplerian circular velocity profile. Models with a low content of dark matter (in particular, most of the *reverse* models) show similar properties.

The model $N = 1857$ ($\Psi = 12$, $a_D = 0.5$, $A_D = 23$, $c_D = 560$, $c_L = 353.7$) has a larger fraction of dark matter ($M_L/M_D = 0.27$), but the dark halo becomes dominant only in the outer regions ($r > r_L$, $r_L = 0.026$, $r_L/r_D = 0.29$). For $0.04\ r_L < r < r_L$ we find $\rho_L \sim r^{-2}$, $\rho_D \sim r^{-1.1}$, while for $r > r_L$, $\rho_L \sim r^{-4}$ and finally for $r > r_D$, $\rho_D \sim r^{-4}$ also. The circular velocity profile has a central peak due to concentration of the luminous component; it stays flat in the region $0.3r_L < r < 1.6r_L$ and begins to decrease at greater radii. Notice how the flat part of the circular velocity profile is produced by the combination of the declining contribution of the luminous component and the rising curve caused by the dark halo.

The model $N = 9382$ ($\Psi = 12$, $a_D = 1.5$, $A_D = 33$, $c_D = 420$, $c_L = 1336$, $r_L = 0.022$, $r_L/r_D = 0.29$) is dominated by dark matter ($M_L/M_D = 0.03$). In the region $5 \times 10^{-3} r_D < r < r_D$ we find $\rho_L \sim r^{-2.7}$, $\rho_D \sim r^{-2}$, while in the outer regions $\rho_L \sim r^{-4}$, $\rho_D \sim r^{-4}$. Outside the inner peak, the circular velocity profile is monotonically decreasing.

Since the transition among these classes of models is smooth, we can identify systems with intermediate features. Models, some of which reverse, with a conspicuous amount of dark matter inside R_e belong to these intermediate categories.

4.3. *Projections along the Line of Sight*

In order to compare theoretical models with observations (as will be done in Paper II), it is necessary to project the relevant physical properties of the models. We have computed the surface density (normalized to the densities at $R = R_e$) and the velocity dispersion profile projected along the line of sight for the luminous and dark component of all the models that we have determined.

For each *normal* model we have computed the parameter χ^2_P

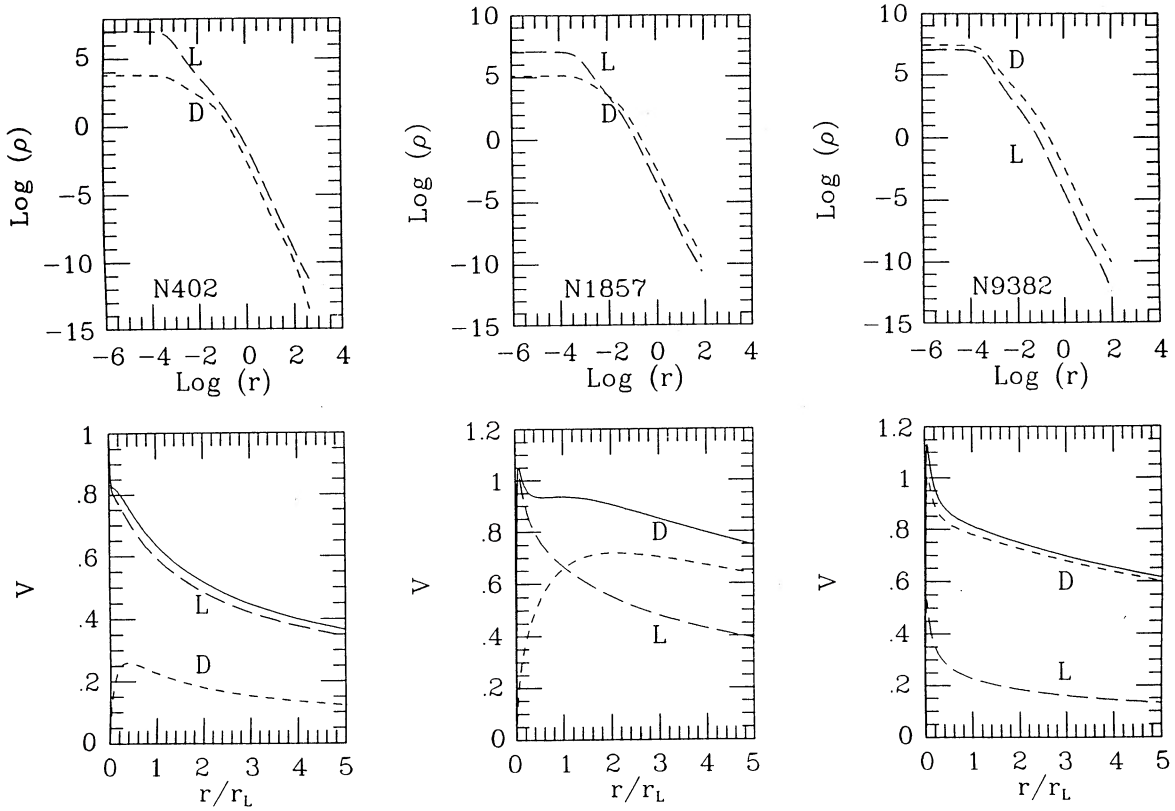

FIG. 2.—Upper row: volume densities of the luminous and of the dark components for three representative models (see discussion in § 4.2). Bottom row: circular velocity profile for the same models separated into the contribution of the luminous and of the dark components. Here the radial distance is normalized to the half-mass radius of the luminous component. All velocities are given in model units.

as a direct measure of the departures from the $R^{1/4}$ law:

$$\chi_P^2 = \sum_{R=R_e/10}^{3R_e} [\mu_L(R) - \mu_{1/4}(R)]^2/N \,, \qquad (9)$$

where $\mu_L = -2.5 \log \Sigma(R)$ is the surface density of the luminous component of the model expressed in magnitudes, $\mu_{1/4}(R)$ is the corresponding magnitude of the $R^{1/4}$ law and N is the number of points considered in the sum. A reasonable correlation is found between χ_P^2 and χ_{10}^2.

In Figure 3 we show the position of the *normal*, minimum-halo (see following § 5) models with $\chi_{10}^2 < 0.01$ on the planes $M_L/M_D - M_L/[R_e\sigma_L^2(0)/G]$ and $M_L/M_D - (M_L$

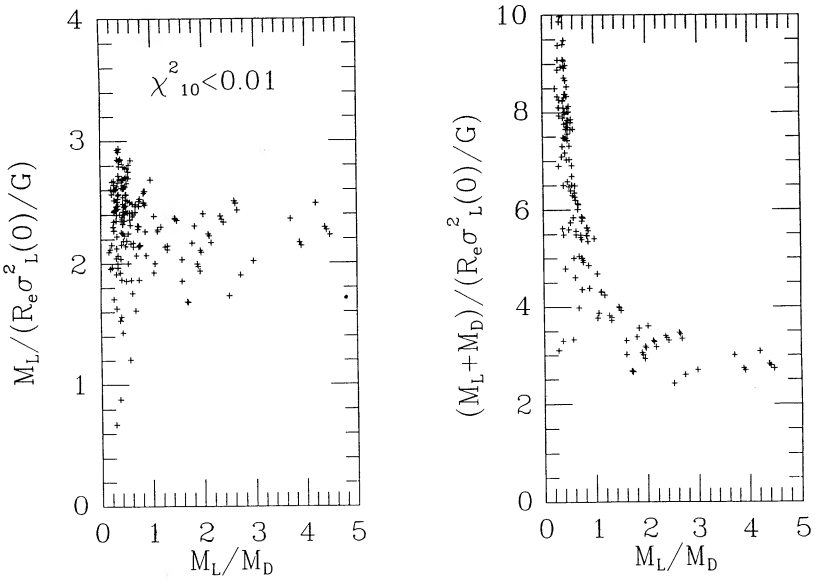

FIG. 3.—Correlations between M_L/M_D and the quantities $M_L/[R_e\sigma_L^2(0)/G]$ (*left frame*) and $(M_L + M_D)/[R_e\sigma_L^2(0)/G]$ (*right frame*) for normal, minimum-halo models with $\chi_{10}^2 < 0.01$. The quantity $R_e\sigma_L^2(0)/G$ clearly underestimates the total mass of the model if $M_L/M_D < 1.5$.

$+ M_D)/[R_e \sigma_L^2(0)/G]$. These plots show that the quantity $2R_e \sigma_L^2(0)/G$, often used to estimate the mass of elliptical galaxies, can give the luminous mass of the objects with $\approx 50\%$ accuracy, but strongly underestimates their total mass, if a massive ($M_L/M_D < 1.5$) dark component is present.

5. MINIMUM-HALO MODELS

There are two obvious limiting cases where significant amounts of dark matter are expected to coexist with the stellar component without distorting the observed luminosity profile. The first possibility is that the dark component is distributed exactly as the luminous component. In this case, only the high value of the derived (constant) M/L ratio may suggest that dark matter is present.

The second and more interesting possibility is to assume that dark matter is diffuse (i.e., $r_D > r_L$), with a central density much smaller than that of the luminous component. In this case, the "dark" contribution to the potential becomes important only in the external regions of the galaxy, and the density distribution of the dark halo is different from that of the stellar component of the galaxy (see, e.g., the model $N = 1857$ described in § 4.2). Here the M/L ratio is an increasing function of radius.

To be more specific, given a two-component model $\bar{f} = \bar{f}_L + \bar{f}_D$ in the self-consistent potential, it is always possible to construct models with the same observables (projected luminosity profile, projected velocity dispersion profile, and circular velocity) but with different amounts of dark matter. For this purpose, it is sufficient to decrease the (M/L) ratio of the stellar component by "moving" part of the mass from the luminous to the dark component:

$$\bar{f} = \bar{f}'_L + \bar{f}'_D = \lambda \bar{f}_L + [\bar{f}_D + (1 - \lambda)\bar{f}_L] , \quad \text{with } 0 \le \lambda \le 1 . \tag{10}$$

This shows that if we find a model $\bar{f} = \bar{f}_L + \bar{f}_D$ that gives a reasonable fit to the data, we can always refer to a model that equally fits the data but has a larger amount of "dark" matter. A few of these models may happen to be well approximated by models of our class, that is, they may have $\bar{f}'_D$ approximated by an f_∞ function.

We note that moving in the opposite direction, that is, that of *increasing* the amount of luminous matter while keeping the same observable profiles is not always possible. If one considers the symmetric procedure defined by exchanging L and D in equation (10), the observable profiles are likely to be changed because we now have $\bar{f}'_L = \bar{f}_L + (1 - \lambda)\bar{f}_D$. On the other hand, if one considers $\lambda \ge 1$ in equation (10), for sufficiently large values of λ the function $\bar{f}'_D$ becomes *negative* and therefore unphysical. On this basis we may define the minimum halo solution for a given object fitted by a model with $\bar{f} = \bar{f}_L + \bar{f}_D$, as that obtained from equation (10) with the largest $\lambda \ge 1$ and $\bar{f}'_D$ positive everywhere. For our $(f_\infty + f_\infty)$-models with $a_L \ge a_D$ and $c_L \ge c_D$ we have

$$\lambda_{\max} = 1 + \frac{A_D}{A_L} \exp\left[-\left(1 - \frac{a_D}{a_L}\right)\Psi \right] . \tag{11}$$

For the models with $c_L < c_D$, $\lambda_{\max} = 1$. The numerical survey has explored models with $\lambda_{\max} \le 6$. Models with high Ψ, low a_D/a_L, or low A_D/A_L values have $\lambda \approx 1$ and consequently have a minimum halo.

Such a minimum halo solution may or may not belong to the class of models investigated in our survey. In any case one should check that the new function $\bar{f}'_D$ does not show peculiar features that would not be reasonably associated with one "homogeneous" component.

5.1. *Limits on the Amount of Dark Matter Inside R_e*

For a class of models for which the luminous component follows the $R^{1/4}$ law and the dark component has a diffuse distribution, we can derive a useful relation between the velocity dispersion profile and the amount of dark matter as a function of radius. In fact, the Jeans equation for the luminous component, under the assumption that the dark component is insignificant at small radii, requires that the central velocity dispersion $\bar{\sigma}_L(0)$ be related to the total mass M_L and to the half-mass radius r_L according to the relation

$$\bar{\sigma}_L^2(0) = \frac{GM_L}{2r_L} . \tag{12}$$

For an $R^{1/4}$ law density profile the density gradient and the cumulative mass profile $M_L(r)$ are also determined. Then the Jeans equation requires

$$GM(r) = 3r\bar{\sigma}_{rL}^2 \left[\frac{2(r_L + 2r)}{3(r_L + r)} - \frac{\alpha}{3} - \frac{1}{3}\frac{d\ln \bar{\sigma}_{rL}^2}{d\ln r} \right] , \tag{13}$$

where $M(r) = M_L(r) + M_D(r)$ and $\bar{\sigma}_{rL}^2 = \langle v_r^2 \rangle_L$. For an $R^{1/4}$ profile we have $r_L \sim 1.32 R_e$ (where R_e is the radius enclosing half of the projected mass), so that $M_L(R_e) \approx 0.43 M_L$. Thus:

$$\frac{M_D(R_e)}{M_L(R_e)} \approx 2.5 \frac{\bar{\sigma}_{rL}^2(R_e)}{\bar{\sigma}_{rL}^2(0)} \left(1 - 0.35\alpha - 0.35 \frac{d\ln \bar{\sigma}_{rL}^2}{d\ln r} \right) - 1 . \tag{14}$$

For many of the models of our survey for $r \lesssim R_e$ we have $\alpha \approx 0$, $d\ln \bar{\sigma}_{rL}^2 / d\ln r \approx -0.5$, and the value of $\bar{\sigma}_{rL}^2(R_e)/\bar{\sigma}_{rL}^2(0)$ exceeds by 15% the value of $\sigma_L^2(R_e)/\sigma_L^2(0)$ for the projected quantities. On this basis we can argue the following estimate:

$$\frac{M_D(R_e)}{M_L(R_e)} \approx 3.5 \frac{\sigma_L^2(R_e)}{\sigma_L^2(0)} - 1 , \tag{15}$$

which now relates the amount of dark matter present inside R_e to the directly observable velocity dispersion profile. Here $\sigma_L(0)$ denotes the velocity dispersion in the vicinity of the center excluding any peculiarities that may be associated with the nucleus. Equation (15) has been derived without assuming any specific form for the distribution functions of the luminous and of the dark components. The only requirements are that the stellar velocity distribution is essentially isotropic in the inner part of the galaxy and that the luminous density follows the $R^{1/4}$ law. Under these hypotheses, a flat velocity dispersion profile traces the presence of a massive dark halo. Note that this estimate of M_D is conservative with respect to the presence of finite rotation of the system, in the sense that, for given observed values of $\sigma_L(R_e)$ and $\sigma_L(0)$, if the object is slightly rotating in the way often observed in ellipticals, then the relation underestimates the $(M_D/M_L)_{R_e}$ ratio.

In Figure 4 we show the properties of the *normal* models of our survey with a projected luminous density that follows with good accuracy the $R^{1/4}$ law ($\chi_{10}^2 < 0.01$) in the plane $\sigma_L^2(R_e)/\sigma_L^2(0)$–$(M_D/M_L)_{R_e}$ Models falling on the relation generally have a diffuse dark component ($r_D > r_L$) with a central density $\rho_D(0)$ much smaller than that of the luminous component. Models with $(M_D/M_L)_{R_e}$ much larger than predicted by equation (15) have instead $\rho_L(0) \approx 1 - 8\rho_D(0)$ and $r_D < 5r_L$. In the central parts of these models the luminous and

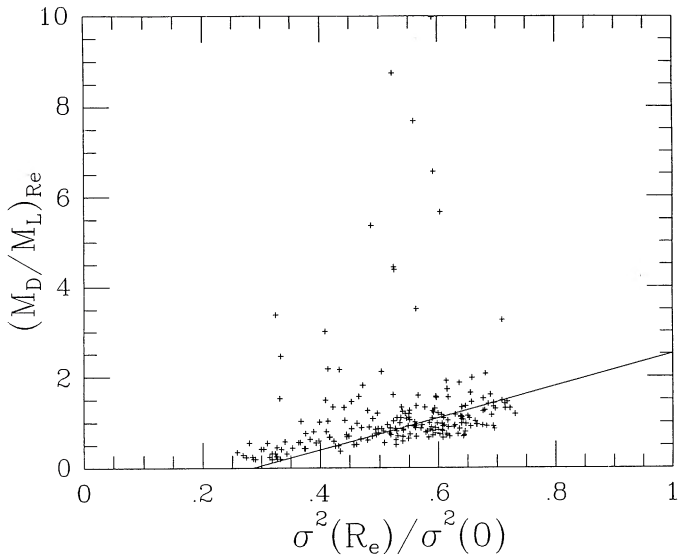

FIG. 4.—Crosses show the normal two-component models with a projected luminosity that follows the $R^{1/4}$ law with a prescribed accuracy ($\chi^2_{10} < 0.01$). The line showing the prediction of eq. (15) is close to the boundary of minimum halo models.

dark density profiles are very close to each other. They have $\lambda_{max} > 1$ and, consequently, following the definition given in § 5, they are not "minimum halo" models.

5.2. *The* $(r_L/r_D, M_L/M_D)$ *Plane*

In order to better characterize the properties of the models of our survey for which the luminous component follows the $R^{1/4}$ law we can refer to the virial relation:

$$2K_L + W_L + W_{LD} = 0\,, \tag{16}$$

where K_L represents the total kinetic energy of the luminous component and

$$W_L = -4\pi G \int_0^\infty r\rho_L(r)M_L(r)dr = -q_L \frac{GM_L^2}{r_L}\,, \tag{17}$$

$$W_{LD} = -4\pi G \int_0^\infty r\rho_L(r)M_D(r)dr = -\frac{GM_L M_D}{r_L}\hat{W}_{LD}\,, \tag{18}$$

represent the gravitational energy terms. The no dark matter case is characterized by $W_{LD} = 0$, $q_L = \frac{1}{2}$. Since the dark component corresponds to a low-Ψ model (if $a_D < a_L$), we may argue that its mass distribution is reasonably represented by a density of the form $\rho_D \propto (r_0^2 + r^2)^{-2}$, with $r_0 \approx 0.45 r_D$. Then we can estimate the interaction term W_{LD} with the following interpolation for the interaction integral:

$$\hat{W}_{LD} \approx \frac{1}{2\pi}\frac{r_L}{r_D}\left[1 + 1.37\left(\frac{r_L}{r_D}\right)\right]. \tag{19}$$

For the class of models that preserve the $R^{1/4}$ law, W_L is practically unchanged with $q_L \approx \frac{1}{2}$, while the presence of the interaction term W_{LD} is balanced by an increase in the kinetic

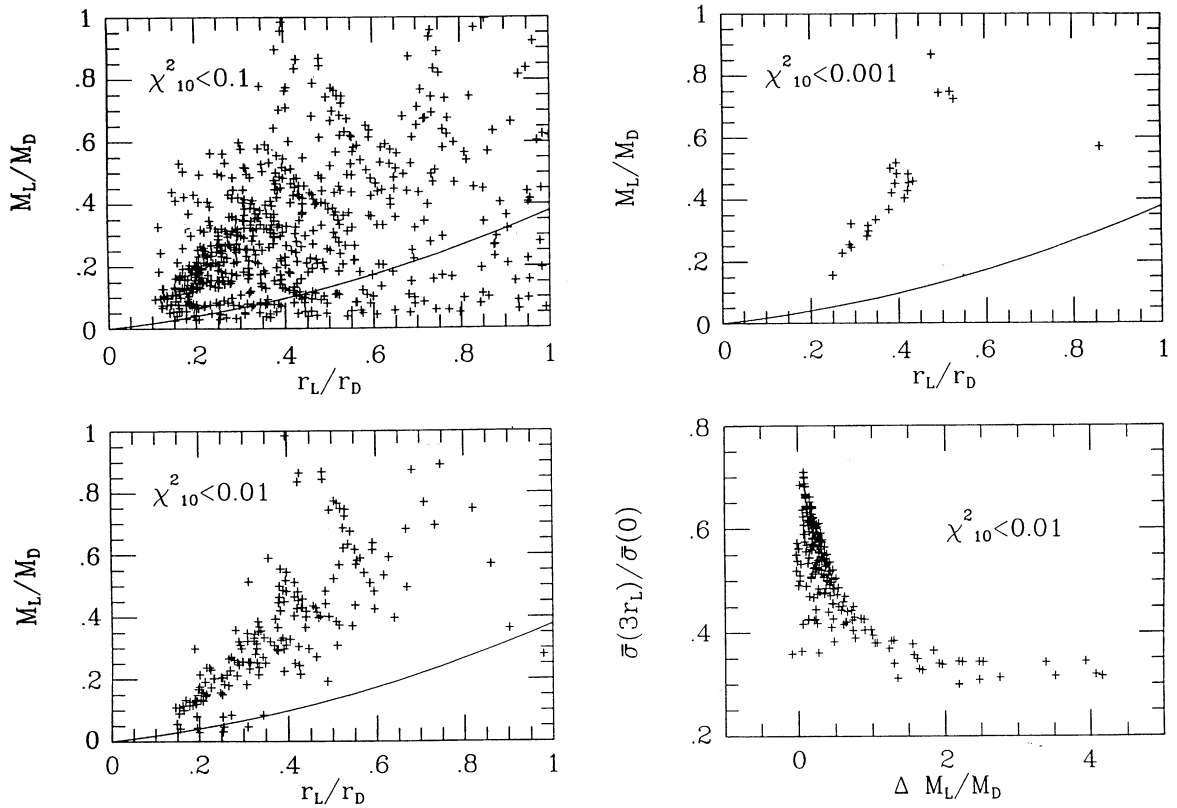

FIG. 5.—Position in the $(r_L/r_D, M_L/M_D)$ plane of the two-component models with a projected luminosity that follows the $R^{1/4}$ law with prescribed accuracy ($\chi^2_{10} < 0.1, 0.01, 0.001$: *upper left*, *bottom left*, and *upper right*, respectively). The line shows the constraint given by eq. (21) argued on the basis of the virial theorem. In the bottom right frame we show the correlation between the difference $\Delta M_L/M_D = M_L/M_D - (M_L/M_D)_{vir}$, where $(M_L/M_D)_{vir}$ is given by the right-hand side of eq. (21), and the flatness parameter of the velocity dispersion profile, for normal models with $\chi^2_{10} < 0.01$. Note that models with low $\Delta M_L/M_D$ values have flatter velocity dispersion profiles.

energy content K_L (see also relation [15]). If we set as an upper limit for K_L the value $(3/2)M_L\bar{\sigma}_{rL}^2(0)$ that would hold for a flat dispersion profile, we obtain the following inequality

$$2K_L = \frac{1}{2}\frac{GM_L^2}{r_L} + \frac{GM_L M_D}{r_L}\hat{W}_{LD} < \frac{3}{2}\frac{GM_L^2}{r_L}, \qquad (20)$$

that is,

$$\frac{M_L}{M_D} > \frac{1}{2\pi}\frac{r_L}{r_D}\left[1 + 1.37\left(\frac{r_L}{r_D}\right)\right]. \qquad (21)$$

Therefore in the $(r_L/r_D, M_L/M_D)$ plane, models following the $R^{1/4}$ law are expected to fall above a parabola, and those models that are close to it are expected to have the flattest velocity dispersion profile (see Fig. 5). The empty region in the upper left part of the plane can be interpreted partly by the limited region of parameter space explored and partly by the fact that those models would have a large interaction term of the luminous on the dark component ($|W_{DL}| \gtrsim |W_D|$). It appears that taking $|W_{DL}| < |W_D|$ goes in the direction of identifying a narrow strip of models that are best fitted by the $R^{1/4}$ law (i.e., $\chi^2_{10} < 0.001$; see Fig. 5, *upper right frame*).

6. CONCLUSIONS

A detailed analysis of the properties of a family of self-consistent, spherical, two-component models of elliptical galaxies has shown that a large set of models exists characterized by the presence of a sizeable amount of dark matter, photometric profiles well-fitted by the $R^{1/4}$ law, and circular velocity and velocity dispersion profiles both fairly flat and featureless.

The distribution function on which the models are based had been shown previously to produce one-component models with the $R^{1/4}$ law as a built-in property (Stiavelli & Bertin 1985). This property is found to be preserved even when the presence of a massive halo is included self-consistently. Both the photometric and the kinematic "conspiracies," neither of which has been imposed a priori, seem to be a natural consequence especially when dark matter has a distribution more diffuse than that of the stellar component.

The present study is mostly based on dynamical arguments on the properties of equilibrium configurations. It remains to be investigated how such equilibria can be obtained as the end product of galaxy formation processes. This line of research is being pursued with the device of N-body simulations.

The models are characterized by a wide range in the ratios of scale lengths and masses, so that their application to the modeling of elliptical galaxies seems to be justified. The major application is to galaxies with dark matter. By fitting the models to observed photometric and kinematical profiles of individual galaxies it is possible to set constraints on the presence and extent of dark halos in these objects. Paper II is devoted to such application.

However, other applications of this approach are possible. The two components may in fact be taken to represent the stellar component and the system of globular clusters in a giant elliptical galaxy, or, alternatively, two different stellar populations in a galaxy with color and metallicity gradients, or, possibly, two distinct stellar populations to represent the observed properties of cD galaxies. Of course for these new cases, the choice of the relevant distribution functions should be carefully examined.

This work has been partially supported by MURST and CNR of Italy. R. P. S. gratefully acknowledges ESO for the hospitality extended to him while part of this work was carried out.

APPENDIX A

NUMERICAL METHODS

The 2939 accepted two-component models described in the paper have been calculated on the VAX 8650 of the Scuola Normale Superiore with a program extensively described by Saglia (1990), with each model identified by a progressive number $N = 2000(i_{a_D} - 1) + 100(i_{c_D} - 1) + 5(i_{A_D} - 1) + i_\Psi$, where $i_{a_D} = 1, 2, \ldots 5$, $i_{c_D} = 1, 2, \ldots 20$, $i_{A_D} = 1, 2, \ldots 20$, $i_\Psi = 1, 2, \ldots 5$, and $a_D(i_{a_D}) = 0.5 + 0.25(i_{a_D} - 1)$, $c_D(i_{c_D}) = 30i_{c_D}$, $A_D(i_{A_D}) = 1 + 2(i_{A_D} - 1)$, $\Psi = 8 + 4(i_\Psi - 1)$.

The Poisson equation is solved by using an iterative shooting method with superlinear convergence. The adopted integration scheme is a fourth-order Adams-Bashfort method (see Press et al. 1985) with a fourth-order Runge-Kutta scheme providing the necessary initialization values. The moments of the distribution functions are computed by using an eight-point Gaussian integrator.

The numerical accuracy of the code has been tested in several ways. Essentially identical results are found by solving the differential equation with the Runge-Kutta method all the way through. Minor changes are observed when the integrations are performed with 12- or 24-point Gaussian integrators. However, the eight-point integrator is probably inadequate for the calculation of very low-density, low-a_D models. In addition, the radial grid used in the calculation has been found to be not sufficiently fine for some of the models with higher central densities and higher Ψ values (i.e., $\Psi = 24$).

The algorithm, when applied to the one-component f_∞ sequence, is able to find correctly the unique value of c associated with a model of given Ψ. The initial guess for c can be varied considerably without affecting the final answer. When applied to the problem of two-component models, the algorithm cannot recognize the possible presence of multiple solutions for c_L. By considering a set of parameters for which two solutions for c_L were known to exist ($a_L = 1.5$, $a_D = 2$, $c_D = 0.1966$, $A_L = 9$, $A_D = 1$, $\Psi = 9$), we have tested that the algorithm can determine one of the two solutions ($c_L = 240$) only when the starting value c_L^s is close to 240 ($239 \leq c_L^s \leq 244$). For other values of c_L^s the algorithm always finds the second solution $c_L = 200$.

For some models with $a_D/a_L = 0.5$–0.68 the code finds solutions with very high values of c_L ($c_L = 10^8$–10^9). Since the f_∞ distribution functions of equations (1) and (2) are set to zero for numerical reasons when the arguments of the exponential functions are lower than -60, these models are certainly inaccurate and have not been considered further in the analysis.

Truncated solutions, with finite radial extent, are easily computed. They have not been considered in the paper since their properties closely resemble those of the models of infinite extent whenever their truncation radius is large. On the other hand, they are not well fitted by the $R^{1/4}$ law when their truncation radius is small.

APPENDIX B

SOME LIMITATIONS OF THE PRESENT SURVEY

A few questions that need to be addressed are related to the effect of adding new ingredients to the physical picture outlined in § 2. An extensive study of these issues is beyond the scope of this paper. Here we report on the properties of some models outside the main survey and on the effect of rotation.

B1. A FEW MODELS OUTSIDE THE MAIN SURVEY

In order to complete our survey, we have also computed a few models with low values of a_D and a few others with $a_D = a_L$. Models with high-velocity dispersion for the dark component (i.e., small a_D) are hard to explore extensively, since they require the use of higher order Gaussian integrators, and consequently large amounts of CPU time. These models tend to have massive and diffuse dark halos and are characterized by very flat circular velocity and velocity dispersion profiles.

Other models outside the main survey have $a_D = a_L$. The interest in these lies in the fact that they represent the case where the dark matter is coldest. The density distribution of the two components is similar for $r < r_L$, so that the mass-to-light ratio is approximately constant at small radii. All the computed models have a massive dark component ($M_L/M_D < 1$). The values of the ratios r_L/r_D and M_L/M_D correlate (see eqs. [7] and [8]), so that massive halos are also diffuse. Only models with $r_L \approx r_D$ or $r_L < 0.1 r_D$ have $\chi^2_{10} < 0.01$, that is, a good $R^{1/4}$ luminosity profile. In their general properties, these models are found to resemble those with $a_D/a_L = 0.75$.

B2. INFLUENCE OF ROTATION

It is possible to construct (spherical) rotating analogues (Petrou 1983) of the models described so far, by using the distribution function discussed in Stiavelli & Bertin (1985, eq. 5.1), and characterized by two additional parameters: B and Ω. Parameter B

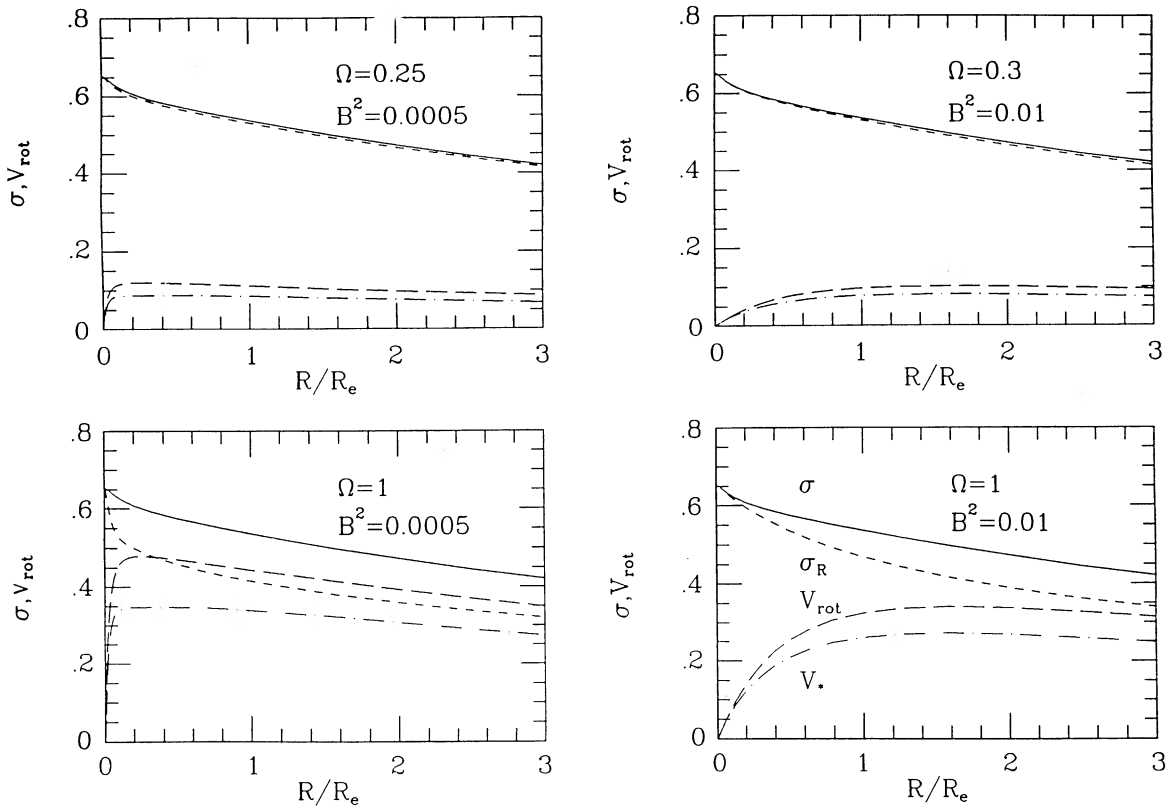

FIG. 6.—Projected rotation curves (*dotted long-dashed lines*) and velocity dispersion profiles (*short-dashed lines*) are plotted for the model $N = 1857R$ modified to include rotation and four values of the parameters defining the rotation curve. The velocity dispersion profile of the nonrotating model (*solid line*) and the unprojected rotation curve (*long-dashed line*) are also shown for comparison. Here the radial distance is normalized to the projected half-mass radius of the luminous component. All velocities are given in model units. Note that the profiles are significantly affected by rotation and projection; in particular, sizeable differences can occur between σ_R and σ, and between V_* and V_{rot}.

defines the shape of the (stellar) rotation curve, and $\Omega(\leq 1)$ the amount of rotation. For the model $N = 1857R$ modified to include rotation, we have computed a few rotation curves for $\Omega = 0.25$, 0.3, 1.0 and for $B^2 = 5 \times 10^{-4}$ and 0.01. These rotation curves are shown in Figure 6 with their projections along a line of sight perpendicular to the rotation axis and with the associated projected velocity dispersions. As is readily seen, models with fast rising rotation curves are characterized by a velocity dispersion profile more peaked toward the center. For Ω close to unity the effect can be quite strong, even when the observed $V_{*\max}/\sigma_L(0)$ is smaller than 0.5.

The influence of rotation on the observed kinematics depends on the specific form of the adopted distribution function. The term $\sigma_L^2(R_e)$ in equation (15) should be replaced by $\sigma_L^2(R_e) + \xi V_*^2(R_e)$, with $\xi \leq 1$. In general, the *measured* mean velocity of the stars V_* would be smaller than the intrinsic unprojected rotation velocity $V_{\rm rot}$, because of the inclination of the axis of rotation with respect to the line of sight, and also as a result of the integration along the line of sight. In addition, the latter effect produces an asymmetric distortion and widening of the line profiles, thus affecting the determination of the velocity dispersion profile (Saglia 1990; Bender 1990).

It is worthwhile to stress that stellar rotation curves, $V_*(R)$, can have a variety of shapes not directly related to the underlying gravitational potential, in contrast to the rotation curve for test particles, such as the H I rotation curve, which is given by the circular velocity $V(R)$ and thus is directly related to the force field.

B3. STABILITY

N-body simulations have been performed to check that the equilibrium models used in this analysis were stable.

REFERENCES

Barnes, J. E. 1989, Nature, 338, 123
Bender, R. 1990, A&A, 229, 441
Bertin, G., Saglia, R. P., & Stiavelli, M. 1988, ApJ, 330, 78
———. 1989, in Astronomy, Cosmology, and Fundamental Physics, ed. M. Caffo et al. (Dordrecht: Kluwer), 303
Bertin, G., & Stiavelli, M. 1984, A&A, 137, 26
———. 1989, ApJ, 338, 723
Binney, J. J., Davies, R. L., & Illingworth, G. D. 1990, ApJ, 361, 78
Canizares, C. R., Fabbiano, G., & Trinchieri, G. 1987, ApJ, 312, 503
de Vaucouleurs, G. 1948, Ann. d'Astrophys. 11, 247
———. 1953, MNRAS, 113, 134
Efstathiou, G., Ellis, R. S., & Carter, D. 1982, MNRAS 201, 975
Fabricant, D., Lecar, M., & Gorenstein, P. 1980, ApJ, 241, 552
Forman, W., Schwarz, J., Jones, C., Liller, W., & Fabian, A. C. 1979, ApJ, 234, L27
Franx, M., & Illingworth, G. 1990, ApJ, 359, L41
Jaffe, W. 1983, MNRAS, 202, 995
Lees, J. F., van Gorkom, J. H., & Knapp, G. R. 1990, BAAS, 21, 1178
Merritt, D., Tremaine, S., & Johnstone, D. 1989, MNRAS, 236, 829
Peletier, R. F., Davies, R. L., Illingworth, G. D., Davis, L. E., & Cawson, M. 1990, AJ, 100, 1091
Petrou, M. 1983, MNRAS, 202, 1209
Press, W. H., Flannery, B. P., Teukolsky, S. A., & Vetterling, N. T. 1985, Numerical Recipes (Cambridge: Cambridge Univ. Press)
Raimond, E., Faber, S. M., Gallagher III, S. J., & Knapp, G. R. 1981, ApJ, 246, 708
Saglia, R. P. 1990, Ph.D. thesis, Scuola Normale Superiore, Pisa
Saglia, R. P., Bertin, G., & Stiavelli, M. 1992, ApJ, 384, 433 (Paper II)
Sancisi, R., & van Albada, T. S. 1987, in Observational Cosmology, ed. A. Hewitt et al. (Dordrecht: Reidel), 699
Sarazin, C. L. 1987, in Structure and Dynamics of Elliptical Galaxies, ed. P. T. de Zeeuw (Dordrecht: Reidel), 179
Schweizer, F., van Gorkom, J. H., & Seitzer, P. 1989, ApJ, 338, 770
Stiavelli, M., & Bertin, G. 1985, MNRAS, 217, 735
———. 1987, MNRAS, 229, 61
Stiavelli, M., & Sparke, L. 1991, ApJ, 382, 466
van Albada, T. S. 1982, MNRAS, 201, 939
van Albada, T. S., Bahcall, J., Begeman, K., & Sancisi, R. 1985, ApJ, 295, 305
van Albada, T. S., & Sancisi, R. 1986, Phil. Trans. R. Soc., Lond., A, 320, 447
van der Marel, R., Binney, J., & Davies, R. L. 1990, MNRAS, 245, 582
van Gorkom, J. H., Knapp, G. R., Raimond, E., Faber, S. M., & Gallagher, J. S. 1986, AJ, 91, 791

THE ASTROPHYSICAL JOURNAL, 384:433–447, 1992 January 10

ELLIPTICAL GALAXIES WITH DARK MATTER. II. OPTIMAL LUMINOUS–DARK MATTER DECOMPOSITION FOR A SAMPLE OF BRIGHT OBJECTS

R. P. SAGLIA[1] AND G. BERTIN
Scuola Normale Superiore, Piazza dei Cavalieri 7, 56126 Pisa, Italy
AND
M. STIAVELLI
European Southern Observatory, Karl-Schwarzschild-Strasse 2, D-8046 Garching bei München, Germany
Received 1991 January 29; accepted 1991 July 22

ABSTRACT

A procedure for the analysis of photometric and kinematical profiles of elliptical galaxies based on a family of spherical, pressure supported, self-consistent two-component models described in a previous paper is developed as a tool to study the presence of dark halos in such systems. Several tests on simulated objects are performed in order to show that this procedure is able to recognize the presence of dark matter, when sufficiently accurate and extended profiles are available; some of these tests have been carried out on flattened objects (E4 and E6), in order to establish how geometry can affect our conclusions. Then we have fitted the most accurate and extended data available for a set of 10 bright nearly round ellipticals. Very good photometric and kinematical fits are obtained; in some of these cases, the preferred models have a massive and diffuse dark component. In general, the amount of dark matter found inside R_e is not too large, of the order of the luminous mass. Typically, the mass-to-light ratio that we derive inside R_e is $M_L/L_B \sim 7\ M_\odot/L_\odot$ for the stellar component, and $(M/L_B)_{R_e} \sim 12\ M_\odot/L_\odot$ for the sum of the two components.

For NGC 4472 the velocity dispersion profile of the best-fit model is found to be well in agreement with the observed kinematics of the globular cluster system; in addition, an analysis devised to assess the statistical significance of the results obtained indicates that the amount of dark matter present in this galaxy exceeds that of the luminous component at a 3 sigma confidence level.

Subject headings: dark matter — galaxies: elliptical and lenticular, cD — galaxies: fundamental parameters — galaxies: kinematics and dynamics

1. INTRODUCTION

In this second paper, devoted to modeling elliptical galaxies with dark matter, we present detailed fits to the photometry and to the velocity dispersion profiles for a set of bright objects. The dynamical basis for the models used in the fitting procedure is given in the first paper (Bertin, Saglia, & Stiavelli 1992, hereafter Paper I), where we have constructed a large data base of fully self-consistent two-component models, characterized by a wide range in the ratios of scale lengths and masses for the luminous and for the dark components. These models are consistent with the most widely accepted physical pictures of galaxy formation, i.e., dissipationless collapse and merging. As a result of the modeling process, for the galaxies under investigation we have determined the gradient of the mass-to-light ratio as a function of radius, i.e., the "optimal" decomposition of the relevant mass distribution into stars and dark matter. For each galaxy, we provide the values for the total luminous mass M_L and for the dark mass M_D as identified by the best-fit models, together with an estimated range of uncertainty on these values.

Some obvious limitations are noted in the approach adopted here. In the first place, the fitting procedure described in § 2, being based on a rather well-defined physical picture of galaxy formation, excludes classes of pressure tensor profiles that would otherwise be admissible for an arbitrary collisionless stellar dynamical equilibrium system. Secondly, the models used, being spherical, fully pressure supported, and based on one simple analytical form for the relevant distribution functions, are expected to provide only an approximate description of the real galaxies.

As to the former limitations, we recognize that other modeling methods that do not make assumptions on the processes of galaxy formation (see Tonry 1983; Richstone & Tremaine 1984), can give important indications on the pressure anisotropy profiles in elliptical galaxies. It should be noted that while a larger intrinsic radial anisotropy would require larger amounts of dark matter, tangential anisotropy could give a flat profile without the need for dark matter. On the other hand, we are not aware of any study of galaxy formation mechanisms able to justify systems with tangential anisotropy and to give quantitative predictions on its profile. However, rather than enter a full discussion of the relative merits of various possible modeling methods, here we would like to show what are the quantitative conclusions that can be drawn from one fitting procedure based on a physically consistent picture, ready to abandon it if it fails to provide satisfactory fits to the observations. In this context, it is crucial to make sure that, *within the assumptions made*, the use of simple models leads to an approximately correct determination of the relevant mass distributions. Thus we have performed several tests in order to set quantitative limits to the application of the adopted fitting procedure. The tests have been performed on simulated observations, by applying our "dynamical diagnostics" to theoretical objects (constructed either analytically or by means of N-body simulations) for which all the intrinsic properties are known in advance (in contrast to real galaxies). As will be

[1] Postal address: Landessternwarte, D-6900 Heidelberg-Koenigstuhl, Germany.

shown in § 3, these tests on simulated observations have been particularly encouraging.

The galaxies studied in this paper (see § 4) have been chosen among the bright objects characterized by fairly round isophotes and by insignificant amounts of rotation. In order to proceed a step beyond a first modeling (see Bertin, Saglia, & Stiavelli 1988, hereafter BSS88; see also van der Marel, Binney, & Davies 1990) where no dark matter has to be invoked, we should refer to a global fit based on cases with accurate and radially extended kinematical profiles (see also Introduction to Paper I). Clearly, accuracy and radial extension cannot be easily improved at the same time, and it is not trivial to assess the proper requirements in order to be able to discriminate between models with and without dark matter with a given confidence level (see discussion in § 3.3). In view of some recently obtained excellent kinematical data (e.g., Davies & Birkinshaw 1988) we have decided to give priority to the accuracy of the data by sacrificing in part the available radial extension. The fits (see § 5) turn out indeed to discriminate between cases where dark matter is required and those where dark matter is not needed. Of course, some issues will be left unresolved until both accurate and radially extended kinematical data will become available (see also Bertin et al. 1989).

The astrophysically interesting results of this study (see §§ 5 and 6) are that in some cases (particularly NGC 4472, 4374, 4636, 7626) we do find, by the adopted fitting procedures, convincing evidence for the presence of dark matter already within the half-light radius R_e; these cases happen to be galaxies that are known X-ray emitters. The case of NGC 4472 is particularly clear, because for this object the identified model with dark matter can naturally account for the observed velocity dispersion in the globular cluster system; in addition, for this object all the models identified at a 3 sigma confidence level (see discussion in § 5.2) have more mass in the dark component than in the luminous component.

2. FITTING PROCEDURE

The set of 2939 accepted two-component models of the main survey described in Paper I is used to fit photometric and kinematic data of elliptical galaxies in a procedure that extends the method described in a previous paper and restricted to models without dark matter (BSS88). For each of the 2939 models of the main survey we produce a fit to a given galaxy by assuming that the projected surface density Σ_L of the luminous component of the model be proportional to the surface luminosity $\mathscr{L}$ of the galaxy, at each location R. This allows us to determine the scale S of the model, i.e., the equivalent in arcsec of the unit length of the model, by minimizing the quantity χ_P^2:

$$\chi_P^2 = \sum_{R_{\min}^P}^{R_{\max}^P} \{[\mu(R) - \mu_L(R/S) + P]/\delta\mu(R)\}^2 . \quad (1)$$

We set $P = -2.5\log(\hat{M}_L/L)$, where the mass of the luminous component $\hat{M}_L$ is expressed in model units. The quantity $\mu(R)$ is the surface brightness (mag arcsec^{-2}) at distance R from the center of the galaxy, $\delta\mu$ is the error on the value of μ, and μ_L is the projected mass density of the luminous component of the model, expressed in magnitudes. The sum extends from $R_{\min}^P$ to $R_{\max}^P$ (see BSS88).

Once the value of S has been determined, the code proceeds to fit the kinematic data (i.e., the velocity dispersion profile of the galaxy). This fit determines the central projected velocity dispersion of the model considered here. The velocity scale S_K is then calculated by minimizing the quantity

$$\chi_K^2 = \sum^{R_{\max}^K} \{[\sigma_{\rm obs}(R) - S_K\sigma_{\rm mod}(R/S)]/\delta\sigma(R)\}^2 , \quad (2)$$

where $\sigma_{\rm obs}$ is the measured velocity dispersion, $\delta\sigma$ the related error, $\sigma_{\rm mod}$ the projected velocity dispersion of the luminous component predicted by the model, $R_{\max}^K$ the maximum radius where kinematical data are available and S is the scale selected by the photometric fit. Therefore we find

$$S_K = \frac{\Sigma\sigma_{\rm mod}(R/S)\sigma_{\rm obs}(R)/\delta\sigma(R)^2}{\Sigma\sigma_{\rm mod}^2(R/S)/\delta\sigma(R)^2} . \quad (3)$$

Finally, the program computes the total luminous mass of the galaxy and the amount of dark matter predicted by the model under study (see BSS88).

We note that in principle the fitting procedure may give different results on the mass content in the galaxy depending on the radial extent of the performed fits, since the scales S and S_K depend on the values of $R_{\max}^P$ and $R_{\max}^K$ considered. Therefore, whenever the data that are fitted cover only a fraction of the half-luminosity radius, as often is the case for accurate CCD data for large nearby objects, one should show that the final conclusions are not too sensitive to the adopted values of $R_{\max}^P$ and $R_{\max}^K$. This point will be considered further in § 3 and in § 5.

We now address the nontrivial issue of defining the best-fit models to a given galaxy and of selecting models within a given confidence level. We may start out by introducing a *global* $\bar{\chi}^2$:

$$\bar{\chi}^2 = \frac{\chi_P^2 + \chi_K^2}{N_P + N_K - 6} . \quad (4)$$

The $\bar{\chi}^2$ parameter is normalized to the total number of data points of the photometric (N_P) and kinematical (N_K) fits, minus the number of parameters (these are the scale S, the velocity scale S_K and the four dimensionless parameters that specify a given two-component model). If N_P and N_K correctly represent the number of independent data points and if $\delta\mu$ and $\delta\sigma$ were Gaussian errors, then $\bar{\chi}^2$ would be a random variable distributed according to the χ^2 distribution of mean 1 and variance $2/(N_P + N_K - 6)$ (see Abramowitz & Stegun 1970). In this case the confidence level of a given fit would be one minus the probability that χ^2 exceeds the actual value of $\bar{\chi}^2$. The selection of models with $\bar{\chi}^2 < 1 + 3\sqrt{2/(N_P + N_K - 6)}$ corresponds to the so-called "3 sigma limit" with confidence level 99.7%. in principle the derived value of $\bar{\chi}^2$ (see eq. [4]) overestimates the real minimum value of $\bar{\chi}^2$, since $\partial\chi_K^2/\partial S \neq 0$, but we have verified that this dependence is very weak. In practice, since the values of the photometric errors are not well under control, it is better to derive S by minimizing only χ_P^2. The resulting values of $\bar{\chi}_P^2$ turn out to be smaller than unity. This prompted us to reassess the significance of the results obtained in terms of *fiducial* photometric errors (see discussion in § 5).

3. TEST OF THE FITTING PROCEDURE ON SIMULATED OBJECTS

In this section we present the results of several tests of the fitting procedure on simulated objects. Our aim is to explore the capabilities of our method to reconstruct the amount and the distribution of dark matter present in a given galaxy (§ 3.1), and to decide whether the method can be applied to systems that are intrinsically nonspherical (§ 3.2). In the last subsection

(§ 3.3) the role played by the accuracy in a given set of data is discussed.

3.1. *Spherical Objects*

We have considered as "test-objects" seven different spherical, self-consistent models with variable amounts and distributions of dark matter and we have applied the fitting program to the projected densities and velocity dispersion profiles of their luminous components. Their physical properties are described in detail by Saglia (1990).

In order to simulate the analysis of excellent but realistic data, the "photometric" fit has been applied to the projected densities (of the luminous component) of the test objects at distances $R_e/10 < R < 4R_e$, while in the kinematical fit only the velocity dispersions (of the luminous component) at distances $R_e/10 < R < R_e$ have been considered. In this analysis no "noise" has been added to the test models: a constant (fictitious) value for the errors $\delta\mu$ and $\delta\sigma$ has been adopted in equations (1) and (2) (see also following § 3.3).

Since for the bright objects studied in the present paper the profiles are radially more restricted, in order to make sure that the results are not too sensitive to the choice of $R^P_{\max}$ and $R^K_{\max}$, we have performed additional tests based on $R^P_{\max} = R_e$ and $R^K_{\max} = R_e/3$, which represents a more common situation. Indeed the results of the fits turn out to be substantially unchanged; but we note that in some of these cases accepted photometric fits can be obtained with differences in the estimated scale length of the test object as large as 50% (see discussion of NGC 4636 in § 5).

From the results of these tests we can draw the following conclusions (see Paper I for some of the terminology used here):

1. The fitting program is able to recognize the presence of dark matter in a given test object, as shown by an examination of the χ^2_P–χ^2_K correlation plots for normal (i.e., with extended and usually more massive halos) and reverse (i.e., with compact and often lighter halos) models.

2. The algorithm is able to derive (within 20%) the scale lengths and the masses of the two components and with a better precision the masses enclosed within R_e only when the dark component is distributed differently from the luminous component, i.e., it is not dominant in the central parts and it is diffuse.

3. The fitting procedure is flexible enough to recognize the presence of dark mass even for systems populated by stellar orbits that are *not* associated with the f_∞-distribution function.

4. If the system under study has a pressure anisotropy profile structure that is drastically different from what is argued on the basis of our physical assumptions, as in the case of a test object heavily populated with radial orbits, then the fitting procedure is still able to get some quantitative answers; however, the quality of the fit is degraded. This means that when dealing with *observed* galaxies our models can be disproved if certain kinematical features turn out to be not well fitted. In contrast, very good kinematical fits are obtained in our sample of bright objects (see § 5).

5. In line with the expectations of some analytical estimates (see Appendix B of Paper I), modest rotation ($V_*/\sigma(o) \simeq 0.13$) does not affect the fits significantly.

To be sure, these conclusions have been drawn only on the basis of the seven cases considered.

3.2. *Flattened Objects*

With the aim of testing the dependence of our diagnostics on the geometry of the system under investigation, we have applied our fitting program to two highly flattened test objects F1 and F2, the first without dark matter, prolate, and characterized by axial ratios 1:3, the second oblate, with dark matter ($M_L/M_D = 0.6$, $r_L/r_D = 0.79$), and with axial ratios 1:2.5. Stellar dynamical models so flattened and characterized by a realistic luminosity profile are presently *not* available in analytical form. Therefore, the test objects have been constructed by means of an N-body code derived from that of van Albada (1982) as described by Bertin & Stiavelli (1989). Model F1 has been produced by simulating galaxy formation via collisionless collapse starting from cold initial conditions. Model F2 instead, has been obtained by a procedure analogous to the one described by Bertin & Stiavelli (1989), by relaxing an approximate flattened configuration. Its evolution has been monitored for about $12t_{\rm cr}$ (defined in terms of the total mass M and the total energy $\mathscr{E}$ as $t_{\rm cr} = GM^{5/2}/|2\mathscr{E}|^{3/2}$) to check that the system actually reached equilibrium.

For each test object, two fits have been performed, one based on simulated observations from a viewing angle that makes the object most flattened (F1E6, F2E4, see Fig. 1) and the other from a viewing angle that makes the object appear roundest (F1E0, F2E0). Of course, it is the second case that applies better to the work presented in this paper, which is devoted to galaxies of the E0–E1 type. For each case the "photometry" of the test object has been derived using the programs described by Bender & Möllenhoff (1987), after smoothing of the projected density of the luminous component. The projected density profile is given as a function of the circularized distance from the center $\sqrt{1-\epsilon}a$, where $1-\epsilon$ is the average axial ratio and a is the distance along the major axis. The quantity ϵ has been set to 0 for test objects F1E0 and F2E0, and to 0.55 and 0.4 for F1E6 and F2E4, respectively. In order to improve the signal to noise ratio of the profiles of test objects F2, four noncorrelated flashes of the N-body configuration have been averaged. A mean velocity dispersion profile has been obtained by averaging the projected velocity dispersion profiles of the luminous component along the major and minor apparent axes of the model and folding the data with respect to the center. The properties of the best-fit models are shown in Figure 2 and the results of the fits are summarized in Table 1. Note that even in these nonspherical cases r_L and r_D refer to *spheres* containing half of the relevant masses. The fits have been performed using constant values of $\delta\mu$ and $\delta\sigma$. From this analysis, the performance of the fits is found to be satisfactory both for the intrinsically prolate F1 and the intrinsically oblate F2 models.

It turns out that better estimates of the physical parameters of the flattened test objects are obtained when these are seen flattened also in projection. Even better results are obtained when the test objects are intrinsically spherical. On the other hand, for intrinsically nonspherical objects seen round in projection, *our method seems to underestimate the amount of dark matter present.* Based on these considerations, we have preferred to focus our attention on E0–E2 galaxies (see §§ 5 and 6).

It has sometimes been argued (see, e.g., Bertola et al. 1991) that the use of spherical models to fit nonspherical objects leads to unreliable results. This is certainly true if kinematical tracers (such as gas) are used that rely on the structure of *closed* orbits. In fact, for these cases one may argue that the structure of these orbits is exceedingly sensitive not only to geometry and viewing angles of the system, but also to the detailed mass distributions (which tends to be badly represented by Stäckel potentials) and especially to figure rotation. The use of the velocity *dispersion profile* of the *stars*, on intuitive grounds, is expected to be less sensitive to the above mentioned factors.

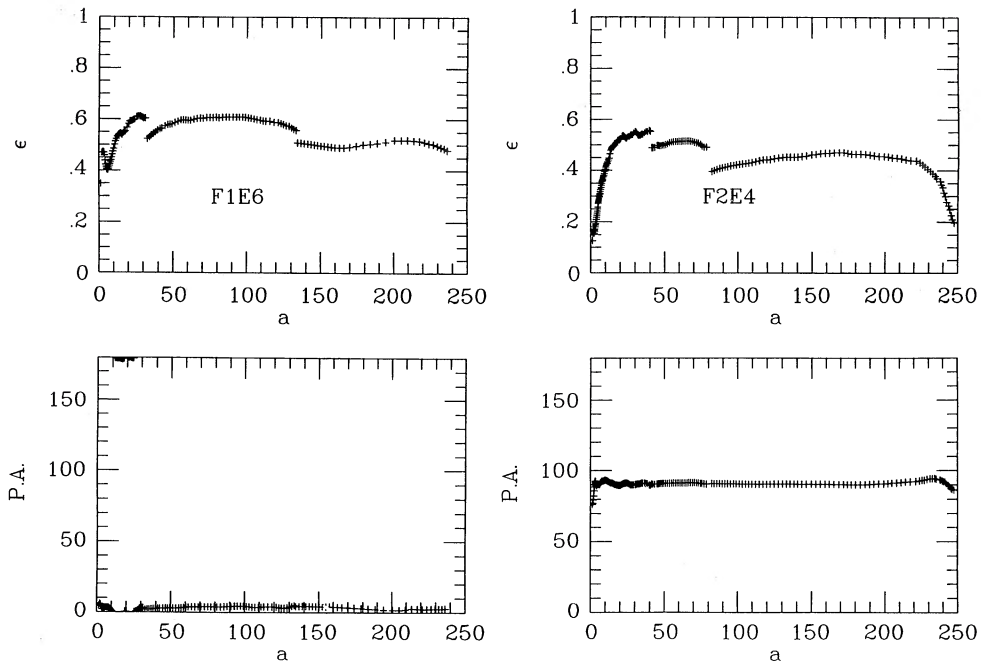

FIG. 1.—Photometric properties of flattened test-objects. The ellipticity ϵ (*top*) and the position angle P.A. (*bottom*) are shown as a function of the radial distance along the major axis a for the models F1 (*left*) and F2 (*right*) seen edge-on. The various profiles extend to $4R_e$. Discontinuities are not intrinsic, but correspond to the use of different smoothings of the data.

This point of view is indeed supported by the simulated observations presented in this subsection.

3.3. *Role of the Accuracy of the Analyzed Data*

All the tests performed so far assume that the photometric and the kinematical profiles are known (at least out to $R^P_{\max}$ and $R^K_{\max}$) with infinite precision. Kinematical profiles are much more noisy than photometric profiles, and only recently stellar kinematics with error bars smaller than 10 km s^{-1} have been derived for some galaxies (see Davies & Birkinshaw 1988), although only out to a fraction of the half-luminosity radius of the galaxies. It is therefore important to examine the role of the accuracy of the analyzed data on the results of the fitting procedure.

The following simple argument can give an estimate of the required precision on the kinematical data for a reliable determination of the amount of dark matter inside R_e. Referring to equation (15) of Paper I, in general we expect to measure a ratio $\mathcal{R}_0 = \sigma_L(R_e)/\sigma_L(0) = 0.53$ if $M_D(R_e) = 0$, and a ratio $\mathcal{R}_1 = 0.76$ if $M_D(R_e)/M_L(R_e) = 1$. So, in order to discriminate between the two cases with a "3 sigma" level of confidence, the error on $\mathcal{R}$ should be smaller than $\delta\mathcal{R} \approx (\mathcal{R}_1 - \mathcal{R}_0)/(3 \times 2) = 0.04$. If we have only two measurements of the stellar velocity dispersion profile, $\sigma_0 \pm \delta\sigma_0$, $\sigma_1 \pm \delta\sigma_1$, where $\sigma_i = \sigma(iR_e)$, we have

$$\frac{\delta\mathcal{R}}{\mathcal{R}} = \sqrt{\left(\frac{\delta\sigma_0}{\sigma_0}\right)^2 + \left(\frac{\delta\sigma_1}{\sigma_1}\right)^2}, \tag{5}$$

and therefore

$$\frac{\delta\sigma_1}{\sigma_1} = \sqrt{\left(\frac{\delta\mathcal{R}}{\mathcal{R}}\right)^2 - \left(\frac{\delta\sigma_0}{\sigma_0}\right)^2}, \tag{6}$$

$$\delta\sigma_1 = \mathcal{R}\sigma_0\sqrt{\left(\frac{\delta\mathcal{R}}{\mathcal{R}}\right)^2 - \left(\frac{\delta\sigma_0}{\sigma_0}\right)^2}. \tag{7}$$

Thus, if $\sigma_0 = (300 \pm 5)$ km s^{-1}, we derive from equation (7) $\delta\sigma_1 = 8$ km s^{-1}, while for $\sigma_0 = (200 \pm 7)$ km s^{-1}, $\delta\sigma_1 = 3$ km

TABLE 1

SIMULATION OF FLATTENED NONROTATING OBJECTS

Model	r_L	r_D	$M_L(R_e)$	$M_D(R_e)$	$M(R_e)$	M_L	M_D	M
F1E0	77				522			1257
Best fit	60				597			1662
Range	57–62				557–618			1521–2055
F1E6	77				522			1257
Best fit	108				505			1406
Range	84–109				409–520			1400–1985
F2E0	72	91	146	338	484	471	785	1257
Best fit	67	96	125	129	254	290	407	697
Range	67–78	70–149	20–180	82–216	236–284	46–416	207–927	623–973
F2 E4	72	91	146	338	484	471	785	1257
Best fit	46	146	194	107	301	459	892	1350
Range	43–46	104–220	62–225	83–217	279–311	145–532	541–1804	1057–1949

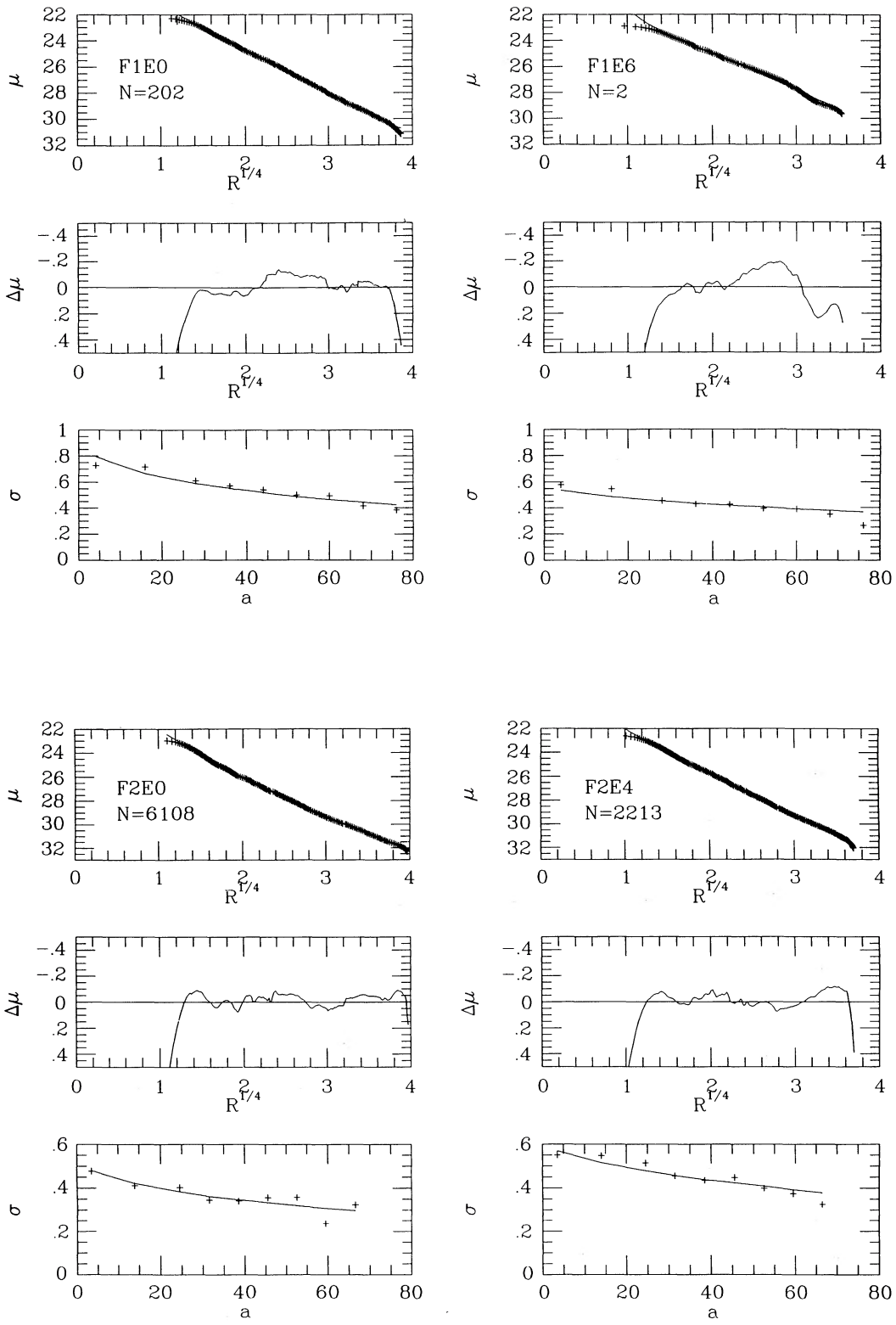

FIG. 2.—Best-fits to the flattened test-objects. The luminosity profiles (*top frames*) of the test objects (*symbols*) are compared to those predicted by the best-fit models (*solid lines*), as a function of the $\frac{1}{4}$ power of the circularized distance from the center (*see text*); the residuals $\Delta\mu = \mu_{obj} - \mu_{mod}$ are shown in the middle frames. The corresponding projected velocity dispersion profiles (*symbols*: test objects; *solid lines*: best-fit model) are given in the bottom frames as a function of the radial distance taken along the major axis *a*.

TABLE 2

GLOBAL PARAMETERS OF THE ANALYZED GALAXIES AND CODING OF THE FITS

Object	Type[a]	D (Mpc)	B_T	Band	FWHM	N_P	$R^P_{\rm min}$	$R^P_{\rm max}$	Source	N_K	$R^K_{\rm max}$	Source	Code
NGC 1399.....	E1P	28	−21.7[b]	R	1″	32	3″.45	66″.26	b	10	37″.3	b	F
				R	1	32	3.45	66.26	b	29	87.9	c	B
				B	1	55	3.1	562	c	29	87.9	c	BSKY
				B	1	82	3.1	3162	c	29	87.9	c	BCLEA
NGC 1404.....	E1	28	−21.36[b]	R	0.9	33	3.1	66.3	b	12	39.4	b	F
NGC 1549.....	E0	23	−21.25[b]	R	1.4	33	3.1	66.3	b	10	50.1	b	F
NGC 3379.....	E1	16	−20.65[d]	B		97	2.7	234	e	10	64.8	f	D
				B		97	2.7	234	e	8	38.6	g	DB
NGC 4278.....	E1	16	−20.01[d]	R	2	32	6.2	118.9	h	8	34.3	g	P
NGC 4374.....	E1	20	−21.43[h]	R	1.6	38	5.5	163.3	h	8	36.3	g	P
				B	2.4	23	5.0	446.6	i	8	36.3	g	MI
				B	2.4	20	5.0	316	i	9	63.3	f, g	MIDBD
NGC 4472.....	E2	20	−22.24[h]	R	2	37	5.4	170.8	h	8	42.8	g	P
				B	3.3	24	5.0	562.3	i	9	63.8	f, g	MI
				B	3.3	41	4.2	316	h, i	9	63.8	f, g	PMI
NGC 4486.....	E0p	20	−22.04[h]	B		185	6.1	1186	j	14	69.7	k	S
				B	1	62	5.47	1186	j, l	8	71.8	g, k	YDBS
NGC 4636.....	E0	20	−21.36[h]	R	2.1	36	5.9	165.3	h	8	37.2	g	P
				B	1.4	9	5.6	316.2	m	9	65.8	f, g	KI
NGC 7626.....	E1p	77	−22.44[b]	r	2	30	3.65	85.05	n	15	34.46	o	K

[a] de Vaucouleurs, de Vaucouleurs, & Corwin 1976.
[b] Franx, Illingworth, & Heckman 1989a, 1989b.
[c] Bicknell et al. 1989.
[d] van der Marel, Binney, & Davies 1990.
[e] De Vaucouleurs & Capaccioli 1979.
[f] Davies 1981.
[g] Davies & Birkinshaw 1988.
[h] Peletier et al. 1990.
[i] Michard 1985.
[j] de Vaucouleurs & Nieto 1978, 1979.
[k] Sargent et al. 1978.
[l] Young et al. 1978.
[m] King 1978.
[n] Kent 1984.
[o] Jedrzejewski & Schechter 1988.

s^{-1}. If N data points have been measured, in the best case we can require the single data points to have error bars lower than $\sqrt{N}\,\delta\sigma_1$. Therefore, better results are obtained if bright galaxies with high central velocity dispersion are considered, since from equation (7) we see that in these cases $\delta\sigma_1$ can be larger.

By performing more realistic (with respect to § 3.1) simulated observations with given Gaussian noise, we find that, since the present accuracy of CCD photometries is of the order of 0.03–0.05 mag arcsec^{-2}, it is possible to recognize unambiguously the presence of an amount of dark matter inside R_e equal to the luminous mass only if the velocity dispersion profile is measured with a precision better than 10% out to such a radius.

4. A SET OF BRIGHT ELLIPTICAL GALAXIES

We now turn our attention to the set of 10 round in projection, slowly rotating ellipticals that have been fitted. Table 2 summarizes the properties of the selected objects, together with the sources for the relevant profiles. Six of these objects have been modeled by us before (BSS88), without dark matter, on the basis of different photometric and kinematical data.

The surface brightness profiles considered in Table 2 have been obtained for the majority of the objects using CCD detectors, with typical accuracy better than 0.1 mag. In a few cases, other (photographic photometry) sources have also been considered in order to cover a larger radial extent. The seeing (FWHM in arcsec) of the various observations is given in Table 2 (except for NGC 3379 and NGC 4486, since the photometries of these objects have been obtained by considering various observations with different seeing conditions), together with the minimum and the maximum radii $R^P_{\rm min}$ and $R^P_{\rm max}$ considered in the photometric fit (see § 2, eq. [1]). The total number N_P of photometric data used in the fit is also given in the table.

As to the kinematics, we have referred to the recent and accurate data derived by Franx, Illingworth, & Heckman (1989b), Jedrzejewski & Schechter (1988), Bicknell et al. (1989), and Davies & Birkinshaw (1988). For NGC 4374, NGC 4472, and NGC 4636 we have performed fits to kinematical profiles obtained by adding to the profiles derived by Davies & Birkinshaw (1988) the last data points measured by Davies (1981). In addition, for NGC 3379 we have considered also the velocity dispersion profile measured by Davies (1981), and for NGC 4486 the extended kinematical data of Sargent et al. (1978). In Table 2 we give for each galaxy the distance from the center of the last available kinematical point $R^K_{\rm max}$, together with the total number of data N_K considered in the fit and the corresponding source. The velocity dispersion profiles taken from Franx, Illingworth, & Heckman (1989b) refer to the major axis of the galaxies and have been folded by considering the data from both sides of the center. The velocity dispersion profile of NGC 1399 has been obtained from Bicknell et al. (1989) by folding and averaging the data points from the two sides of the

center (along the major axis):

$$r = \frac{r_+ + r_-}{2} \tag{8}$$

$$\sigma(r) = \left(\frac{\sigma_+}{\delta\sigma_+^2} + \frac{\sigma_-}{\delta\sigma_-^2}\right) \Big/ \left(\frac{1}{\delta\sigma_+^2} + \frac{1}{\delta\sigma_-^2}\right) \tag{9}$$

$$\delta\sigma(r) = 1 \Big/ \sqrt{\frac{1}{\delta\sigma_+^2} + \frac{1}{\delta\sigma_-^2}} \,. \tag{10}$$

Here r_+ and r_- are the distances of the points on the two sides of the galaxy ($r_+ \approx r_-$), σ_+ and σ_- the relative values of the velocity dispersions, and $\delta\sigma_+$ and $\delta\sigma_-$ the error bars. The data in the inner 5″ have been excluded (see discussion in the following § 5). The last two points have been measured on the western side of the galaxy only. The velocity dispersions given by Davies & Birkinshaw (1988) are averaged over all slit position angles. Finally, the velocity dispersion profile for NGC 7626 (Jedrzejewski & Schechter 1988) has been obtained by folding and averaging the velocity dispersion data measured along the two sides of the major axis of the galaxy as for the data of Bicknell et al. (1989) (see eqs. [8]–[10]). The sets of data used for the fits (photometry and kinematics) are listed in Table 2 and there identified by a code in the last column.

5. THE FIT

To each set of data of Table 2 we have applied the fitting procedure described in § 2 using a constant value for the photometric errors ($\delta\mu = 0.1$ mag arcsec^{-2}). For each case we have selected all the normal and reverse models with χ_P^2 and χ_K^2 parameters lower than some prescribed values. These upper limits have been chosen (somewhat arbitrarily, see following § 5.2) to be of the order of or lower than the values of χ_P^2 and χ_K^2 derived from the one-component (i.e., $M_D = 0$) f_∞ fits (in Table 3 we report the results of such fits), which have been carried out for the purpose of comparison. Among the selected models we have identified a "best-fit" solution, by trying to minimize both the χ_P^2 and the χ_K^2 parameters (further discussion is given in § 5.2).

In Tables 4–7, the first column of the tables identifies the objects, while in the second column the code specifies the data used in the fit (see Table 2), with an additional N to indicate fits by normal models. For each code two rows are reported: the first gives the parameters of the selected "best-fit," the second the ranges for the acceptable fits. In Table 4, the "range" row for χ_P^2 and χ_K^2 gives the upper limits adopted in the selection. In Table 5, $M(R_e)$ is the value of the spherical mass enclosed inside R_e. Only the properties of the best-fit cases are summarized in the tables; complete data on all the fits performed are listed by Saglia (1990). The global values of M/L_B are not actually reliable, given the limited range of the kinematical profiles available. For the same reason, it would have been fairer to record the values of $(M/L_B)_{R^K_{\max}}$, i.e., referred to the sphere sampled by the kinematical data, but we have preferred to list the values of $(M/L_B)_{R_e}$ which have an easier physical interpretation and are more easily compared to one another.

For all the 10 galaxies considered here we have obtained good fits of their photometric and kinematical data, by considering models with a dark component. The selected models illustrated in the figures have always χ_P^2 smaller than the number of data points. In general the quality of the kinematical fit is also very good. Figure 3 shows the photometric and kinematical best fits for eight of the ten galaxies. The luminosity excesses in the center would have been removed if we had performed the appropriate seeing convolution.

We may summarize the conclusions that can be drawn from the analysis of these fits by saying that we find no evidence for dark matter in NGC 1549, marginal evidence in NGC 1399, NGC 1404, NGC 3379, NGC 4278, NGC 4486, and relatively good evidence in NGC 4374, NGC 4472, NGC 4636, and NGC 7626, for which the two components fits improves significantly upon one component fits. In our view the most convincing case for dark matter is that of NGC 4472.

In many cases (NGC 4472, NGC 4636, NGC 7626) the obtained evidence is for massive ($M_L/M_D < 0.5$) and diffuse ($r_L/r_D < 0.5$) halos (see Table 6), with modest amounts of dark matter inside $R_e[(M_L/M_D)_{R_e} > 1]$. In three cases where X-ray data are available, we observe a correlation between the extent of X-ray emission and the derived halo scalelength. For NGC 4374 we have found best-fit models that have significant amounts of dark matter even inside R_e.

For the cases of NGC 4374 and NGC 4472, which in our view provide the strongest evidence for the presence of dark matter, the results of the fitting procedure are illustrated separately in more detail (similar plots have been produced for all the other galaxies of Table 2; see Saglia 1990). For NGC 4472, in Figure 4 we show the correlation plots χ_P^2–χ_K^2 obtained for normal and reverse models separately (fits PMIN and PMIR). Only normal models minimize the parameters χ_P^2 and χ_K^2 and these have a diffuse dark halo. The set of identified models at a 3 sigma level (see following § 5.2) is represented in Figure 5 in the (r_L/r_D, M_L/M_D) physical plane (see Paper I, Fig. 5). In Figure 6 we show for the best-fit solution the fit to the photometric profile, the residuals $\Delta\mu \doteq \mu - \mu_{\rm mod}$, and the fit to

TABLE 3

FIT BY ONE-COMPONENT f_∞ MODELS[a]

Object	Code	χ_P^2	χ_K^2	Ψ	R_e	r_M	M	$(M/L_B)'$
NGC 1399.....	B	17.7	40.5	30	51″	67″	5.2	7.0
NGC 1404.....	F	9	53.9	6	91.2	120	4.8	8.8
NGC 1549.....	F	6.5	44.1	25	76	101	2.7	5.5
NGC 3379.....	DB	55.3	9.9	30	65	84	1.5	5.2
NGC 4278.....	P	9	8.1	6	110	144.9	2.7	17.2
NGC 4374.....	P	13.7	53.2	25	69	92.6	5	8.6
NGC 4472.....	P	4.2	65.8	12	131	172.3	8.8	7.2
NGC 4486.....	YDBS	81.9	5.7	12	132	173	8.9	8.7
NGC 4636.....	P	6.8	38.5	7.7	229	300.7	5.4	9.9
NGC 7626.....	K	3.4	119	9.6	45	59.6	7.8	5.3

[a] Masses are in $10^{11}\,M_\odot$, and M/L ratios are in solar units.

TABLE 4

RESULTS OF THE TWO-COMPONENT FITS TO THE GALAXIES OF TABLE 2

Object	Code	χ^2_P	χ^2_K	R_e(Kpc)	R_e	r_L	r_D
NGC 1399.....	BN	3.53	6.91	13.6	100″.0	135″.6	838″.5
	BN	7.50	9.00	9.8–13.6	72.1–100.0	97.8–136.0	654.0–838.5
NGC 1404.....	FN	6.04	60.50	8.3	61.5	89.6	91.1
	FN	7.75	69.30	4.6–9.5	34.1–69.8	46.2–108.0	85.3–395.9
NGC 1549.....	FN	2.43	37.91	9.5	85.1	114.6	420.3
	FN	3.10	56.70	9.5–11.2	85.1–100.0	114.6–134.7	396.8–671.3
NGC 3379.....	DBN	59.76	5.12	4.8	61.5	82.9	167.9
	DBN	59.85	7.00	4.4–5.0	56.4–64.1	75.8–86.6	128.1–450.1
NGC 4278.....	PN	3.36	7.31	4.4	57.1	78.1	480.2
	PN	6.00	11.20	4.4–7.8	57.1–100.0	78.1–148.8	95.6–492.1
NGC 4374.....	PN	1.99	4.51	12.6	130.0	179.2	184.3
	PN	2.88	7.00	7.1–18.1	73.6–186.7	99.9–264.5	163.1–366.7
NGC 4472.....	PMIN	5.89	5.04	12.0	123.9	166.2	466.1
	PMIN	9.75	12.64	10.3–14.6	106.5–151.0	142.3–204.4	385.9–1266.1
NGC 4486.....	YDBSN	66.14	2.72	13.1	134.8	181.3	379.5
	YDBSN	82.60	2.80	12.6–13.1	129.6–134.8	175.1–181.3	178.8–448.3
NGC 4636.....	PN	6.70	4.06	15.6	160.8	214.9	1277.2
	PN	6.80	5.60	15.6–19.4	160.8–200.0	214.9–267.7	861.9–1517.7
NGC 7626.....	KN	1.70	29.51	15.3	40.9	54.6	353.2
	KN	2.24	35.00	14.9–15.3	39.9–41.1	53.3–54.9	320.5–382.3

the velocity dispersion profile. Note that we have incorporated in the kinematical profile the velocity dispersion data points of the globular clusters obtained by Mould et al. (1990). The predictions of the best-fit model (identified on the basis of the stellar data alone) are found to be well consistent with the data out to $R = 300'' \approx 2.5R_e$. In Figure 7 we show more in detail the results of the optimal luminous-dark decomposition for the mass distribution of NGC 4472, in terms of volume densities, cumulative masses, and force fields as measured by the circular velocity profile V; in addition, in this composite figure we show the gradient of the cumulative mass-to-light ratio. In Figures 8 and 9 we show the analogous plots obtained for NGC 4374 (data PN).

5.1. *Detailed Discussion of Individual Objects*

5.1.1. *NGC 4374*

This galaxy of the Virgo cluster is known as a radio and an X-ray source with X-ray emission measured out to $R_X \simeq R_e$ (e.g., Sarazin 1990). We have fitted both the photometric profiles of Peletier et al. (1990) and of Michard (1985). A proper matching of the two photometries is impossible, since they have different slopes. The best-fit models selected using the two

TABLE 5

RESULTS OF THE TWO-COMPONENT FITS TO THE GALAXIES OF TABLE 2[a]

Object	Data	$M_L(R_e)$	$M_D(R_e)$	$M(R_e)$	M_L	M_D	M
NGC 1399.....	BN	2.5	1.5	4.0	5.9	37.3	43.2
	BN	2.0–2.5	1.0–1.9	3.1–4.2	4.8–5.9	30.2–37.5	35.7–43.2
NGC 1404.....	FN	1.1	1.5	2.6	2.5	4.0	6.5
	FN	0.8–1.6	0.5–1.9	1.6–2.9	1.8–3.7	3.3–6.8	5.5–10.2
NGC 1549.....	FN	0.7	1.0	1.7	1.7	6.3	8.0
	FN	0.7–1.0	0.9–1.3	1.7–2.2	1.7–2.4	6.3–12.8	8.0–15.1
NGC 3379.....	DBN	0.6	0.4	1.0	1.4	1.9	3.3
	DBN	0.5–0.7	0.3–0.5	1.0–1.1	1.3–1.7	1.1–5.0	2.8–6.3
NGC 4278.....	PN	0.8	0.2	1.1	2.0	3.7	5.7
	PN	0.2–0.9	0.2–1.6	1.1–1.8	0.5–2.2	1.7–4.5	2.8–6.0
NGC 4374.....	PN	1.8	2.7	4.6	4.2	6.9	11.1
	PN	0.3–2.1	1.7–4.4	3.0–6.5	0.7–4.9	4.9–15.6	9.7–17.4
NGC 4472.....	PMIN	3.3	1.7	5.1	7.9	13.4	21.3
	PMIN	2.6–3.6	1.3–3.2	4.4–6.5	6.0–8.4	8.4–49.6	16.7–56.8
NGC 4486.....	YDBSN	3.3	1.7	5.0	7.8	9.0	16.8
	YDBSN	2.8–3.4	1.3–2.0	4.5–5.1	6.6–8.1	4.1–9.8	10.7–17.1
NGC 4636.....	PN	2.4	0.9	3.3	5.9	22.5	28.4
	PN	2.0–2.8	0.9–2.5	3.3–4.5	4.8–6.6	11.0–38.5	17.4–43.4
NGC 7626.....	KN	3.3	1.2	4.6	8.1	38.0	46.1
	KN	3.3–3.4	1.2–1.5	4.5–4.8	7.9–8.2	30.3–47.2	38.3–55.3

a Masses are in $10^{11} M_\odot$.

TABLE 6

RESULTS OF THE TWO-COMPONENT FITS TO THE GALAXIES OF TABLE 2

Object	Code	$\frac{r_L}{r_D}$	$\left(\frac{M_L}{M_D}\right)_{R_e}$	$\frac{M_L}{M_D}$
NGC 1399.....	BN	0.2	1.6	0.2
	BN	0.1–0.2	1.3–2.4	0.1–0.2
NGC 1404.....	FN	1.0	0.7	0.6
	FN	0.2–1.0	0.5–2.9	0.3–0.8
NGC 1549.....	FN	0.3	0.8	0.3
	FN	0.2–0.3	0.7–1.1	0.2–0.3
NGC 3379.....	DBN	0.5	1.5	0.7
	DBN	0.2–0.6	1.2–2.7	0.3–1.5
NGC 4278.....	PN	0.2	4.0	0.5
	PN	0.2–1.0	0.1–4.0	0.1–0.8
NGC 4374.....	PN	1.0	0.7	0.6
	PN	0.3–1.1	0.1–1.2	0.0–1.0
NGC 4472.....	PMIN	0.4	2.0	0.6
	PMIN	0.1–0.5	0.9–2.7	0.1–1.0
NGC 4486.....	YDBSN	0.5	2.0	0.9
	YDBSN	0.4–1.0	1.6–2.7	0.7–1.6
NGC 4636.....	PN	0.2	2.7	0.3
	PN	0.2–0.3	0.8–2.7	0.1–0.6
NGC 7626.....	KN	0.2	2.7	0.2
	KN	0.1–0.2	2.2–2.7	0.2–0.3

photometries are different. Larger values of r_L are generally found using the photometry of Peletier et al. (1990; fits P). However, the selected *normal* and *reverse* models have all substantial amounts of dark matter for both photometries. Dark matter is present in significant amounts even inside R_e.

5.1.2. *NGC 4472*

NGC 4472 is the brightest galaxy in the Virgo cluster. It is a radio and an X-ray source with very extended X-ray emission (out to $R_X \simeq 4R_e$, see, e.g., Sarazin 1990). As for the previous object, NGC 4374, we have considered both photometries of Peletier et al. (1990) and Michard (1985). In this case it is possible to match the two sets of data, so we have extended the photometry of Peletier et al. (1990) with the last 5 data points of Michard (1985). *Reverse* models are not able to minimize both the χ_P^2 and the χ_K^2 parameters (see Fig. 4). The selected (*normal*) models have a large fraction of dark matter, but this is in the form of a diffuse halo. In the central regions of the galaxy the amount of dark matter present is low. The scale length of the dark halo is much larger than the scale length of the luminous component. Note how the selected best-fit model (see Fig. 6) has a velocity dispersion profile well consistent with the data derived from the globular cluster system of the galaxy (Mould et al. 1990) out to $R \approx 2.5R_e$.

5.1.3. *NGC 4636*

This galaxy of the Virgo cluster is known to be a radio and an X-ray source with X-ray emission extending to about $R_X \simeq 2R_e$ (e.g., Sarazin 1990). It would be desirable to supplement the photometric profile of Peletier et al. (1990) with more extended data. Unfortunately, a proper matching with the King (1978) photometric profile is not easy to perform. Large differences (50%) are found in the derived half-mass radii using the two photometries. In any case, it is not possible to minimize both χ_P^2 and χ_K^2 parameters for *reverse* models. The selected *normal* models have all a massive and diffuse dark halo. The invisible halo has a scale length many times larger than the scale length of the stellar (luminous) component of the galaxy. We conclude that we find evidence for a diffuse massive dark halo embedding NGC 4636.

5.1.4. *NGC 7626*

NGC 7626 is the brightest galaxy of Pegasus I. It has a shell structure and peculiar central stellar kinematics. It is known as a radio and an X-ray source. The velocity dispersion profile of this galaxy is peculiar, so that the quality of the kinematical fits

TABLE 7

RESULTS OF THE TWO-COMPONENT FITS TO THE GALAXIES OF TABLE 2 AND COMPARISON WITH ONE-COMPONENT [$(M/L_B)'$] FITS AND OTHER AUTHORS[a]

Object	Code	$\frac{M_L}{L_B}$	$\left(\frac{M}{L_B}\right)_{R_e}$	$\frac{M}{L_B}$	$\left(\frac{M}{L_B}\right)'$	Other
NGC 1399.....	BN	8	12.8	58.0	7	5.1–8.2[b]
	BN	6.5–8.0	9.7–13.2	48.0–58.0		
NGC 1404.....	FN	4.6	10.8	12	8.8	
	FN	3.3–6.7	6.8–12.4	10.1–18.8		
NGC 1549.....	FN	3.5	8.1	16.2	5.5	
	FN	3.5–4.9	8.1–10.7	16.2–30.6		
NGC 3379.....	DBN	5	8.4	11.7	5.2	6.3[c]
	DBN	4.6–6.0	8.0–9.4	9.7–22.2		
NGC 4278.....	PN	12.5	15.7	36.1	17.2	11[c]
	PN	3.0–13.8	15.7–25.5	18.0–38.3		
NGC 4374.....	PN	7.2	17.9	19.2	8.6	11–19[d]
	PN	1.1–8.4	12.2–25.3	16.8–30.0		
NGC 4472.....	PMIN	6.5	9.8	17.4	7.2	8.9[c], 6.5–86[d]
	PMIN	4.9–6.9	8.6–12.4	13.6–46.4		
NGC 4486.....	YDBSN	7.7	11.6	16.5	8.7	
	YDBSN	6.4–7.9	10.2–11.7	10.5–16.7		
NGC 4636.....	PN	10.8	14.8	52.1	9.9	9.2–120[d]
	PN	8.9–12.1	14.8–19.8	31.9–79.7		
NGC 7626.....	KN	5.5	7.5	31.3	5.3	
	KN	5.4–5.6	7.4–7.9	26.0–37.5		

[a] Mass-to-light ratios are given in solar units.
[b] Bicknell et al. 1989.
[c] van der Marel, Binney, & Davies 1990.
[d] Katz & Richstone 1985.

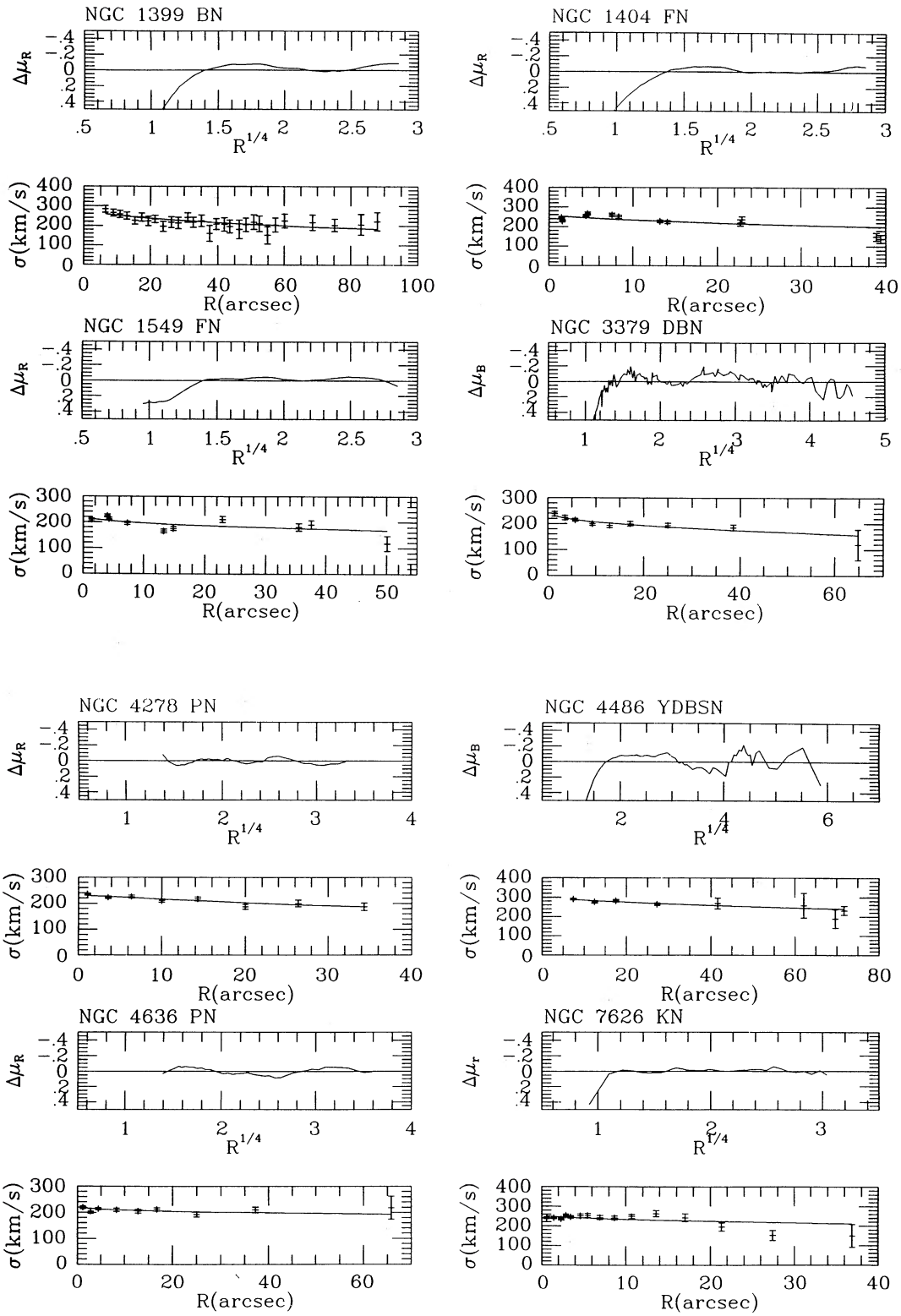

FIG. 3.—Best-fits to eight elliptical galaxies (all the galaxies of Table 2, with the exception of NGC 4374 and NGC 4472). For each galaxy two frames are shown based on the data and on the best-fit model identified by the relevant codes: the residuals $\Delta\mu = \mu - \mu_{\rm mod}$ (*top*: $\Delta\mu > 0$ implies that the model is more luminous than the galaxy), and the velocity dispersion profiles (*bottom*: data points carry error bars). For NGC 3379 and NGC 4636 an additional outer data point taken from Davies (1981) has been added to the data of Davies & Birkinshaw (1988).

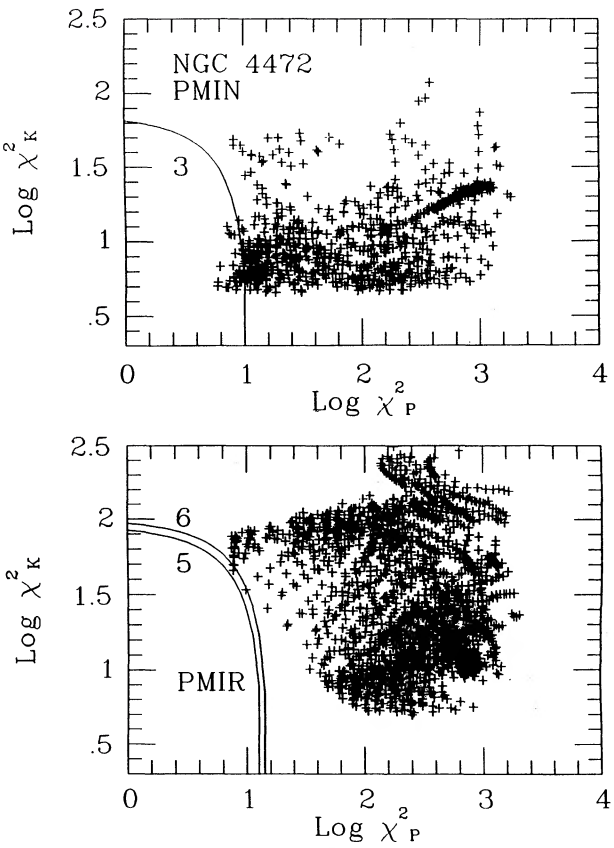

FIG. 4.—Correlation between χ^2_P and χ^2_K for NGC 4472 (*top*: normal models; *bottom*: reverse models). On the basis of these diagrams reverse models are excluded at 5 sigma level and the models accepted with 99.7% confidence level (3 sigma) have all substantial amounts of dark matter ($M_D > M_L$, see Fig. 5). Contours labeled by n identify the n sigma limit.

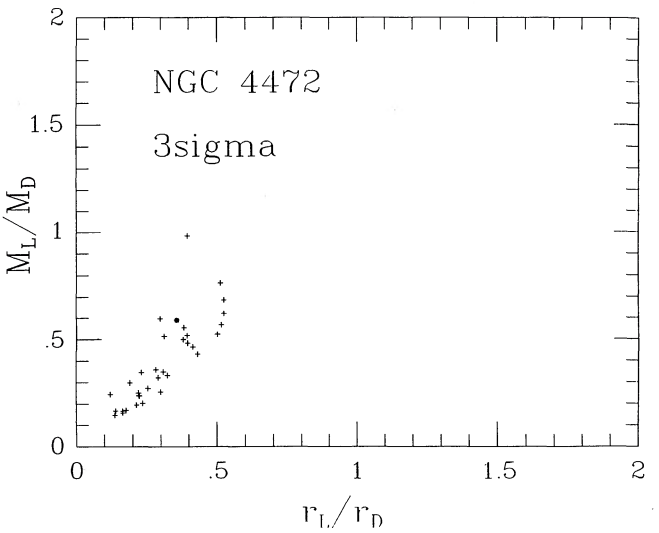

FIG. 5.—Set of identified models at a 3 sigma level (see Fig. 4) is represented in the physical plane (r_L/r_D, M_L/M_D) for NGC 4472. The point marked by a special symbol identifies the best-fit model $N = 418$.

is always low, with high values of χ^2_K. The best photometric and kinematical fits are obtained with *normal* models. *Reverse* models have in general higher values of χ^2_K. These selected (*normal*) models have a large fraction of dark matter, quite diffuse: the scale length of the dark halo is 4–8 times larger than that of the luminous component. We conclude that also for NGC 7626 there is evidence for a massive and diffuse dark halo, but caution is required by the unusual kinematics displayed by this object.

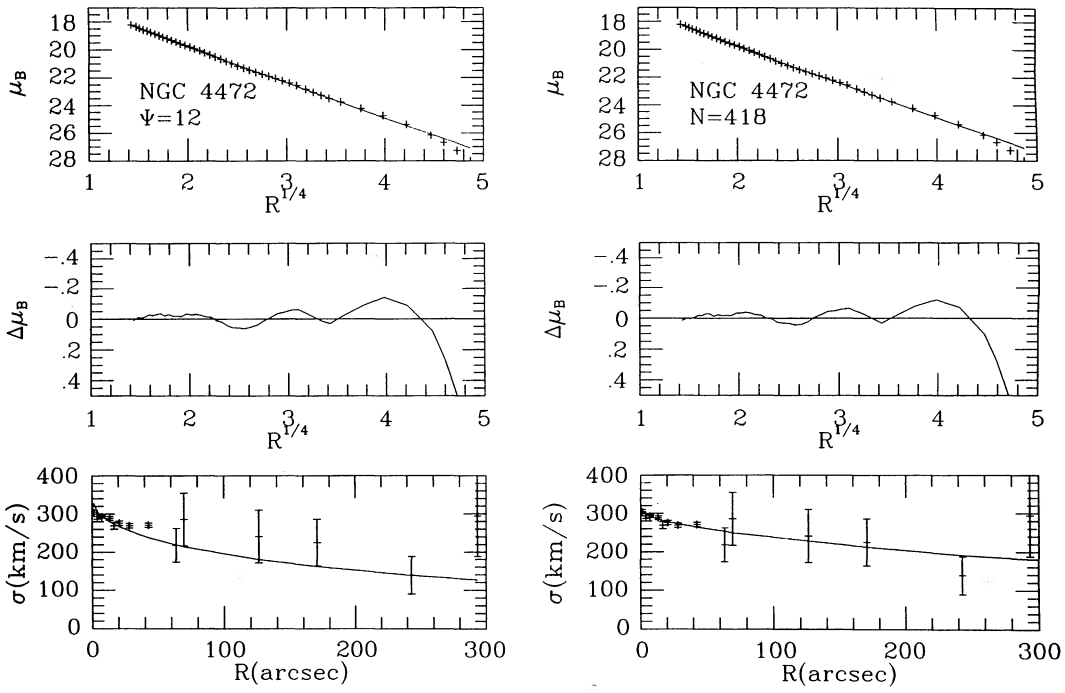

FIG. 6.—Best-fits to NGC 4472 with (*right*: model $N = 418$) and without (*left*: model $\Psi = 12$) dark matter, for the data PMI. Luminosity profiles are at the top, photometric residuals in the middle, and velocity dispersion profiles at the bottom. The five outermost kinematic data points refer to the globular cluster system (see text).

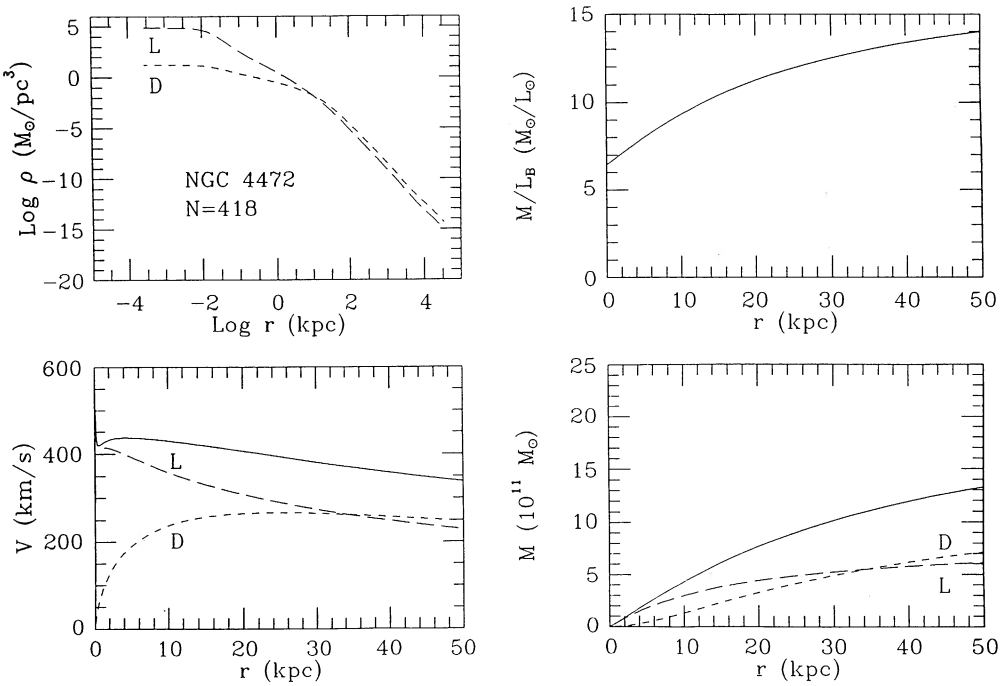

FIG. 7.—Intrinsic properties of the best-fit model ($N = 418$) for NGC 4472 (data PMI). Volume densities (*top left*), circular velocity profile decomposition (*bottom left*), mass-to-light ratio (*top right*), and integrated mass (*bottom right*). Solid lines identify global quantities, long-dashed lines refer to the luminous component, and short-dashed lines to the dark component. The model clearly belongs to the second class of models described in Paper I (§ 4.2; see middle frames of Fig. 2). Note how the two components "conspire" to give a fairly flat circular velocity profile.

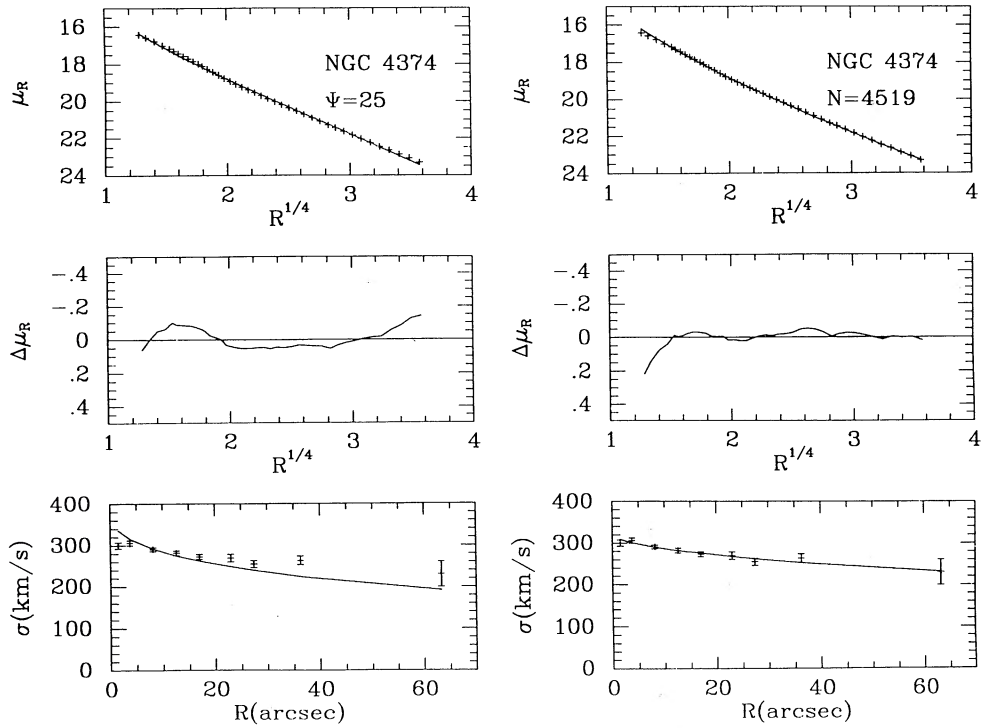

FIG. 8.—Best-fits to NGC 4374 with (*right*: model $N = 4519$) and without (*left*: $\Psi = 25$) dark matter, for the data *P*. Frames are shown as in Fig. 6.

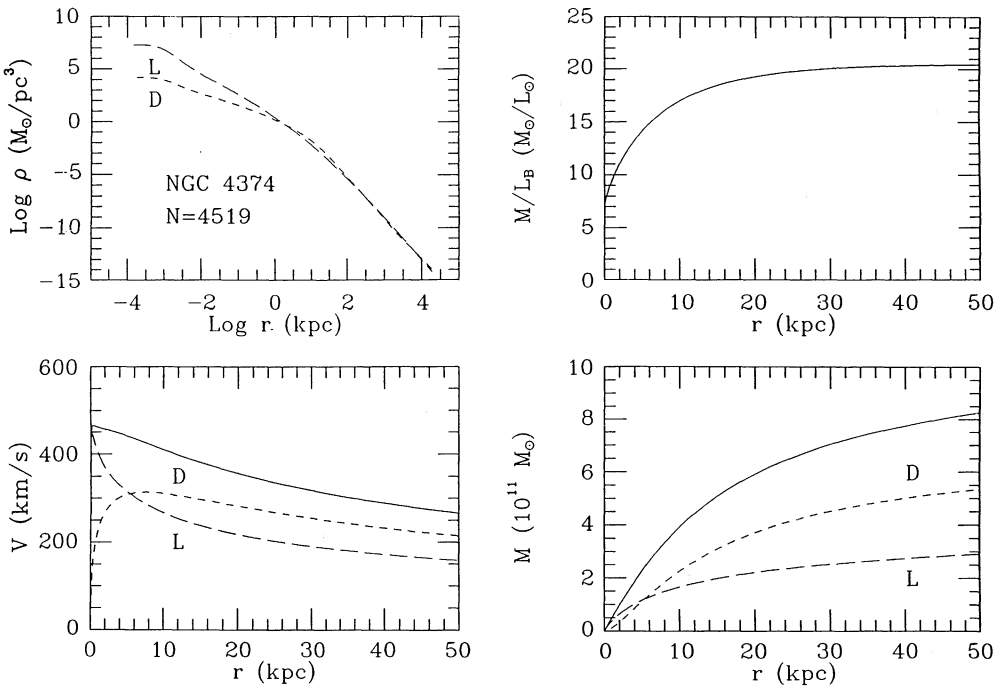

FIG. 9.—Intrinsic properties of the best-fit model ($N = 4519$) for NGC 4374 (data P). (See Fig. 7 for a description of the frames). This model belongs to a class of models intermediate between the first and the second of those described in Paper I (§ 4.2; see left and middle frames of Fig. 2). Here the two components have similar scale lengths so that the resulting circular velocity profile is not flat, and the mass-to-light ratio "saturates" the global value of 19 at $r \approx 20$ kpc.

5.2. *The Statistical Significance of the Results*

Some words have to be spent on the selection of the "best-fit" models. If we exclude the special cases of NGC 1399 and M87, where models with extended dark halos have been selected by taking into account that the peculiar kinematics of the central regions has increased the final value of χ_K^2, the upper limits for χ_P^2 and χ_K^2 have been chosen to be of the order of or lower than the values of χ_P^2 and χ_K^2 derived from the $M_D = 0$ one-component fit. Note that the photometric fit alone fixes "approximately" four of the six parameters that specify a two-component model. Indeed, by selecting models with a χ_P^2 value lower than a given limit, we isolate a more or less narrow region in the $(r_L/r_D, M_L/M_D)$ plane (see Fig. 5 of Paper I). The kinematical fit limits this permitted region further. Therefore, while the one-component photometric and kinematical fits have two and one free parameters respectively, the two-component photometric and kinematical fits have "approximately" four and two free parameters, respectively. If we compare $\hat{\chi}_P^2$ and $\hat{\chi}_K^2$ (the χ_P^2 and χ_K^2 values normalized to the relevant number of the degrees of freedom, see Tables 2, 3, and 4), we see the following. The values of $\hat{\chi}_P^2$ are usually lower than 1, since our constant value of the photometric error (0.1 mag arcsec^{-2}) is likely to overestimate the real errors on the data (a more realistic estimate of the photometric errors is described in the following) and also because the number of photometric data exceeds the actual number of independent data points. In the cases of NGC 4374, NGC 4472, and NGC 4636 only models with massive dark halos give $\hat{\chi}_K^2$ values lower than the "3 sigma" limit. Therefore, for these galaxies there is evidence for dark mass. For NGC 7626 models with massive halos have $\hat{\chi}_K^2$ lower by a factor of 2 than models without dark mass. From this statistical point of view, for the other galaxies the evidence for the existence of dark halos is less convincing.

Actually, a more rigorous selection from a statistical point of view (say, select all the models with a given "confidence level") is hard to implement, since the statistical meaning of the obtained values for the global $\bar{\chi}^2$ parameter (see eq. [4]) is hard to assess, given the uncertainties on the photometric error $\delta\mu$ and the number of independent data points. In addition, since usually we have $N_P \gg N_K$, the value of $\bar{\chi}^2$ is bound to measure the quality of the photometric fit only. This means that when it is possible to find models that minimize both χ_P^2 and χ_K^2 quantities, these minimize also $\bar{\chi}^2$, but models that give bad kinematical fits can nevertheless have a low $\bar{\chi}^2$ value. On the other hand, using photometric errors greater than or equal to 0.1, one derives values of $\bar{\chi}^2$ that are well below unity for the majority of the models. Consequently, if in many of the cases analyzed it is possible to identify a "best-fit" model, it is very hard to select rigorously a set of equally plausible models and thus to compute the relevant range of values for the physical parameters.

In an effort to overcome some of these difficulties, we have introduced a fiducial photometric error $\overline{\delta\mu}$ for a given galaxy by imposing that:

$$\bar{\chi}_f^2 = \frac{\chi_P^2(\delta\mu^2/\overline{\delta\mu^2}) + \chi_K^2}{N_P + N_K - 6} \geq 1 , \qquad (11)$$

for all the models considered in the fit. In doing this we have in mind that the actual photometric errors are smaller than usually assumed, consistent with the small point to point scatter in the profiles. In general we find $\overline{\delta\mu} \simeq 0.05$.

Using the derived values of $\overline{\delta\mu}$ as photometric errors, we have repeated the selection of the best-fit models and found that in the majority of cases they include the models selected according to the intuitive prescription mentioned before. However, the number of acceptable solutions within a nominal "3 sigma" confidence level is generally large and so is the

allowed range for the derived physical parameters. Only in the already mentioned cases of NGC 4472 and NGC 7626 the "3 sigma" limit excludes reverse models and requires $M_L/M_D < 1$. Since the kinematical profile of NGC 7626 is peculiar (see previous discussion), we claim a "3 sigma" detection of dark mass only for NGC 4472. For this galaxy *reverse* models are excluded at the 5 sigma level (see Fig. 4). The ranges of the parameters derived imposing the 3 sigma level do not differ significantly from those given in Tables 4–7 (see Fig. 5). Here we note that three of the models selected by the 3 sigma level are on the boundary of the parameter space covered by the set of 2939 accepted two-component models of the main survey (see Paper I). However, our conclusions are not expected to change if the fitting procedure is applied on a larger "data base" of two-component models, because models for which the dark component is too diffuse and not sufficiently massive would also be excluded on the basis of the simple argument given in Paper I (see § 5.1, especially eq. [15]). In fact, models selected by the photometric fit and with fairly flat velocity dispersion profile tend to cluster in a narrow strip in the $(r_L/r_D, M_L/M_D)$ plane (see eq. [21] and Fig. 5 of Paper I); in addition, we have checked that for NGC 4472 one-component ($M_D = 0$) models are rejected at the 7.4 sigma level.

Referring to the discussion of minimum halo models given in Paper I (§ 5), we note that all the best-fit models are often close to the relevant minimum halo solution (Paper I, eq. [15]); for NGC 4472 the minimum halo solutions compatible with the "3 sigma" requirement have $M_D \geq M_L$ (see Fig. 5).

6. M/L RATIOS

We now turn to the final discussion of our results and of their implications on the problem of dark matter in elliptical galaxies. The picture that the luminous stellar component of elliptical galaxies (see also discussion in Paper I) is usually embedded in a fairly massive and diffuse dark halo is supported by the results of our fits (see especially NGC 4472 and the cases of NGC 4636 and NGC 7626). However, we should reiterate that if this is indeed the real situation there is no way to make a stronger and more convincing case for the presence of dark matter in elliptical galaxies until accurate but, especially, extended kinematical data become available. Thus, not unexpectedly, one of the strongest cases of the present survey of ellipticals is that of NGC 4374 which appears to have a considerable amount of dark matter but *not* in diffuse form.

The M/L ratios derived from our best-fit models are listed in Table 7. If we exclude NGC 4278 (for this galaxy there can be a problem of distance determination) the derived values of the mass-to-light ratio for the luminous component M_L/L_B are not too large, (3–11 $M_\odot/L_\odot$ with mean value 7), while the values for the sum of the two components referred to the sphere of radius R_e, $(M/L_B)_{R_e}$, are in the range 7–18 (mean value 12). All these numbers refer to the "best-fit" *normal* models. In contrast, the *global* (M/L_B) can be very large, up to 50 $M_\odot/L_\odot$. Note also that the mass-to-light ratios derived from one-component fits $(M/L_B)'$ (see Table 3) are usually intermediate, i.e., $M_L/L_B < (M/L_B)' < M/L_B$. Finally, we should stress that these values for the M/L ratios are based on the Hubble constant $H = 50$ km s^{-1} Mpc^{-1} (see Sandage & Tammann 1990, and references therein); they would double if we set $H = 100$ km s^{-1} Mpc^{-1}.

In Table 7 we also list for comparison the M/L ratios obtained in other dynamical studies; note that the authors of the first and second reference consider the same kinematical data as those analyzed in this paper. The axisymmetric models of van der Marel, Binney, & Davies (1990) are characterized by (constant) M/L ratios that are slightly smaller than our $(M/L_B)_{R_e}$ ratios. Bicknell et al. (1989) find that an isotropic spherical model can explain the observed velocity dispersion profile of NGC 1399 if the M/L ratio increases with radius; alternatively, taking a constant M/L ratio requires that the stellar orbits become more tangential in the outer regions. The two numbers reported in Table 7 correspond to eastern and western kinematical profiles (for the constant M/L fits). Finally, we note that our results are within the ranges predicted by Katz & Richstone (1985) obtained for spherical isotropic models from an application of linear programming techniques in the presence of dark halos; their values are referred to the sphere of radius R_e.

In one respect our conclusions on the amount of dark matter present are on the *conservative* side. In fact, if galaxies were largely populated with radial orbits, as is sometimes argued by dynamicists, then the current data would already imply very large amounts of dark matter inside R_e.

7. CONCLUSIONS

The results of this paper add evidence to the picture that elliptical galaxies can be embedded in massive diffuse dark halos and suggest that dark matter can be present in significant amounts even inside the half-luminosity radius.

It has often been noted that stellar kinematical data may be explained without having to invoke the presence of dark matter if the underlying orbital structure is properly chosen, on a case by case basis; these arguments leave unresolved the physical justification of the various orbital structures that are found. In contrast, here we have shown that, under *simple physical assumptions* that lead to a well defined framework for stellar orbits, remarkably good fits are obtained by *fully self-consistent models*, and that these fits are able to discriminate cases where dark matter is required (and its amount is estimated) and cases where the data are well explained by one-component models. The impact of many limitations intrinsic to the adopted fitting procedure has been evaluated by means of extensive tests on simulated objects and good overall support to the method used has been found.

A considerable effort has also been made in order to give statistical significance to the results obtained, i.e., to establish a confidence level for the estimates of the amounts of dark matter derived for the objects of our survey. At least in one case, that of NGC 4472, we find that within our physical assumptions dark matter must be present ($M_L < M_D$) with a 3 sigma confidence level. Of course, statements of this kind are hard to make because the nature and the size of errors and the number of independent parameters in the fit of photometric and kinematical data are not fully under control. Even more severe limitations to making a strong statement on the presence of dark matter derive from the fact that the analyzed data are not as accurate and as radially extended as desired. In this latter respect, our best-fit models should be strengthened and improved upon by considering additional kinematical tracers, such as X-rays and the globular cluster system. In fact, the objects where we have the strongest indications for the presence of dark matter are also well-known X-ray sources; for the case of NGC 4472 the matching with the kinematical data of the globular cluster system is remarkable.

General trends in the amount and distribution of dark matter are hard to establish, given the small sample of objects

studied in this paper. A marginal correlation between amount of dark matter and size should be confirmed by application to smaller elliptical galaxies and to larger sets of fitted objects with confidence level comparable to or better than that obtained here for NGC 4374 and NGC 4472. In the near future stellar dynamical studies of this kind, coupled with studies of other kinematical tracers on statistically significant samples of ellipticals should be able to lead to solid statements of cosmological interest.

We thank R. Bender for providing his programs for the analysis of the photometries of flattened models. We also thank R. Bender, R. Davies, and G. Efstathiou, for stimulating discussions and comments. This work has been partially supported by MURST and CNR of Italy. R. P. S. gratefully acknowledges ESO for the hospitality extended to him while part of this work was carried out. Part of the work has been carried out by R. P. S. in Oxford, as external ESA fellow.

REFERENCES

Abramowitz, M., & Stegun, I. A. 1970, Handbook of Mathematical Functions (New York: Dover)
Bender, R., & Möllenhoff, C. 1987, A&A, 177, 71
Bertin, G., Saglia, R. P., & Stiavelli, M. 1988, ApJ, 330, 78 (BSS88)
———. 1992, ApJ, 384, 423 (Paper I)
Bertin, G., et al. 1989, ESO Messenger, 56, 19
Bertin, G., & Stiavelli, M. 1989, ApJ, 338, 723
Bertola, F., Bettoni, D., Danziger, I. J., Sadler, E. M., Sparke, L. S., & de Zeeuw, P. T. 1991, ApJ, 373, 369
Bicknell, G. V., Carter, D., Killeen, N. E. B., & Bruce, T. E. G. 1989, ApJ, 336, 639
Davies, R. L. 1981, MNRAS, 194, 879
Davies, R. L., & Birkinshaw, M. 1988, ApJS, 68, 409
de Vaucouleurs, G., & Capaccioli, M. 1979, ApJS, 40, 699
de Vaucouleurs, G., & Nieto, J.-L. 1978, ApJ, 220, 449
———. 1979, ApJ, 230, 697
de Vaucouleurs, G., de Vaucouleurs, A., & Corwin, H. G. 1976, Second Reference Catalogue of Bright Galaxies (Austin: Univ. Texas Press)
Franx, M., Illingworth, G., & Heckman, T. 1989a, AJ, 98, 538
———. 1989b, ApJ, 344, 613
Jedrzejewski, R. I., & Schechter, P. L. 1988, ApJL, 330, L87
Katz, N., & Richstone, D. O. 1985, ApJ, 296, 331
Kent, S. M. 1984, ApJS, 56, 105
King, I. R. 1978, ApJ, 222, 1
Michard, R. 1985, A&AS, 59, 205
Mould, J. R., Oke, J. B., de Zeeuw, P. T., & Nemec, J. M. 1990, AJ, 99, 1823
Peletier, R. F., Davies, R. L., Illingworth, G. D., Davis, L. E., & Cawson, M. C. 1990, AJ, 100, 1091
Richstone, D. O., & Tremaine, S. 1984, ApJ, 286, 27
Saglia, R. P. 1990, Ph.D. thesis, Scuola Normale Superiore, Pisa
Sandage, A., & Tammann, G. A. 1990, ApJ, 365, 1
Sarazin, C. 1990, in The Interstellar Medium in Galaxies, ed. H. A. Thronson & J. M. Shull (Dordrecht: Kluwer), 201
Sargent, W. L. W., Young, P. J., Boksenberg, A., Shortridge, K., Lynds, C. R., & Hartwick, F. D. A. 1978, ApJ, 221, 731
Tonry, J. L. 1983, ApJ, 266, 58
van Albada, T. S. 1982, MNRAS, 201, 939
van der Marel, R., Binney, J., & Davies, R. L. 1990, MNRAS, 245, 582
Young, P. J., Westphal, J. A., Kristian, J., Wilson, C. P., & Landauer, F. P. 1978, ApJ, 221, 721